5-2017

Hot Filament Chemical Vapor Deposition of Semiconducting Boron Carbide Thin Films

Michael Dylan Richardson
University of Tennessee, Knoxville, mricha30@vols.utk.edu

To the Graduate Council:

I am submitting herewith a thesis written by Michael Dylan Richardson entitled "Hot Filament Chemical Vapor Deposition of Semiconducting Boron Carbide Thin Films." I have examined the final electronic copy of this thesis for form and content and recommend that it be accepted in partial fulfillment of the requirements for the degree of Master of Science, with a major in Nuclear Engineering.

Eric D. Lukosi, Major Professor

We have read this thesis and recommend its acceptance:

Lawrence H. Heilbronn, Maik K. Lang

Accepted for the Council:
Dixie L. Thompson

Vice Provost and Dean of the Graduate School

(Original signatures are on file with official student records.)

Hot Filament Chemical Vapor Deposition of Semiconducting Boron Carbide Thin Films

A Thesis Presented for the
Master of Science
Degree
The University of Tennessee, Knoxville

Michael Dylan Richardson
May 2017

ACKNOWLEDGEMENTS

Thank you to Dr. Eric Lukosi for his support during my undergraduate and graduate education. Thank you to Mr. Scott Emert for training me on various tools in the machine shop. Thank you to Dr. Kyung-Min Lee for performing Silvaco simulations. Thank you to Dr. Heilbronn and Dr. Lang for providing feedback and suggestions and for being on my thesis committee. Finally, thank you to my loving family and fiancée for supporting me while pursuing a higher education.

ABSTRACT

A highly efficient, low-power, compact thermal neutron detection system with excellent gamma-ray discrimination is desired for a number of applications. ^{10}B [boron-10] has a large cross section for thermal values and a Q-value of 2.78 MeV. For this reason, investigations into boron carbide, boron nitride, and boron phosphide semiconductor neutron detectors are underway. Because boron carbide has the highest fraction of boron of the three, it holds the highest potential. With this in mind, a hot filament chemical vapor deposition (HFCVD) system was designed and built in order to grow thin films of boron carbide onto n-type silicon substrates. Deposition was accomplished via the thermal decomposition of B_2H_6 [diborane] and CH_4 [methane].

TABLE OF CONTENTS

LIST OF TABLES

LIST OF FIGURES

CHAPTER ONE

INTRODUCTION

Background Information

Although the first boron carbide compound was discovered in 1858, it was not studied in detail until 1934. It was initially discovered as a byproduct of a reaction involving metal borides, with Joly preparing B_3C in 1883 and Moissan preparing B_6C in 1894 [1, 2]. The stoichiometric ratio of B_4C came about in the 1930s—albeit some controversy remained on the exact stoichiometry [1]. Because of its unique combination of properties, boron carbide is used in a wide array of engineering applications. Its high melting point (>2400°C), thermal stability, low density (2.52 g/cm^3), and high hardness allow for it to be used in various industries—from refractory applications to semiconductor applications [1]. A low density, high chemical inertness, and high neutron capture cross section all make boron carbide an attractive material for nuclear, medical, space, military, and micro-electronic applications [3]. All of these properties make boron carbide a useful material in semiconductor technology as well, especially solid-state radiation detectors [1].

Boron carbide is a refractory material and exists as a stable, single-phase compound, with the carbon concentrations ranging from 8 up to 20 at.% [3]. The rhombohedral boron carbide structures are the most stable, with this including the following stoichiometry: $B_{13}C_2$, $B_{12}C_3$, or B_4C. Other phases close to $B_{12}C_3$ may also be considered rhombohedral. According to early work by Lagrenaudie, boron carbide is a p-type semiconductor, even at very high temperatures [1, 3]. Several groups have estimated the band gap of boron carbide, with these values ranging from nearly 0.5 eV up to around 2 eV, which is smaller than typical ceramic semiconductor values [1]. This range of values exists because the electrical and mechanical properties of the material are dependent upon the boron and carbon concentrations in the material. Much larger band gaps (e.g., 3 eV or greater) are found for boron carbide in theoretical band structure calculations; however, these calculations likely do not adequately account for the disorder in the material that could give rise to mid-gap states [1].

Theory

Boron trifluoride (BF_3) and helium-3 (^{3}He) gas-filled detectors are widely used in neutron detection [4]. However, ^{3}He is becoming short in supply, while BF_3 has limited application because of its toxicity. A semiconductor-based neutron detector is a possible alternative to these gas-filled detectors for applications not requiring a large area detection system. Additionally, due to a sensing medium with a higher density, these semiconductor-based detectors are inherently more efficient than BF_3 and ^{3}He detectors. In order for these detectors to have a high detection efficiency, however, a high purity

and a single-crystalline growth (e.g., single-crystalline boron carbide) are required [5]. Fortunately, many groups have investigated the growth of single-crystalline boron carbide.

Semiconductors and Radiation Interaction

As previously discussed, boron carbide is a p-type semiconducting material. This means that it has an excess of electron acceptor sites in the bulk material, with holes being the majority carrier and dominating the electrical conductivity [5]. Because boron carbide is p-type, it needs to be deposited onto an n-type semiconducting material in order to form a p-n heterojunction. A simplified version of a p-n junction can be seen in Figure 1, with the depletion region, electric field, and forces acting on the charged carriers being seen in Figure 2 [6]. At the metallurgical junction, there is initially a very large density gradient in both electron and hole concentrations, with majority carrier electrons diffusing into the p-region and majority carrier holes diffusing into the n-region [6]. Assuming no external bias, this process cannot continue forever. Electrons leave behind positively charged donor atoms in the n region, while holes leave behind negatively charged acceptor atoms. The net positive and negative charges in the two regions then induce an electric field near the metallurgical junction. This electric field goes from the positive to the negative region, as seen in Figure 2. The net positively- and negatively-charged regions shown in Figure 2 form the depletion region, which is also known as the space charge region. By assuming no external bias across the p-n junction, the junction is in thermal equilibrium, with the Fermi energy level constant throughout the system [6].

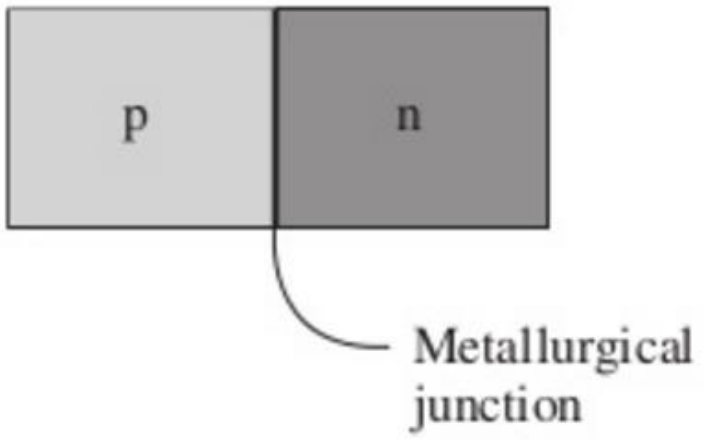

Figure 1: Simple geometry of an ideal p-n junction [6].

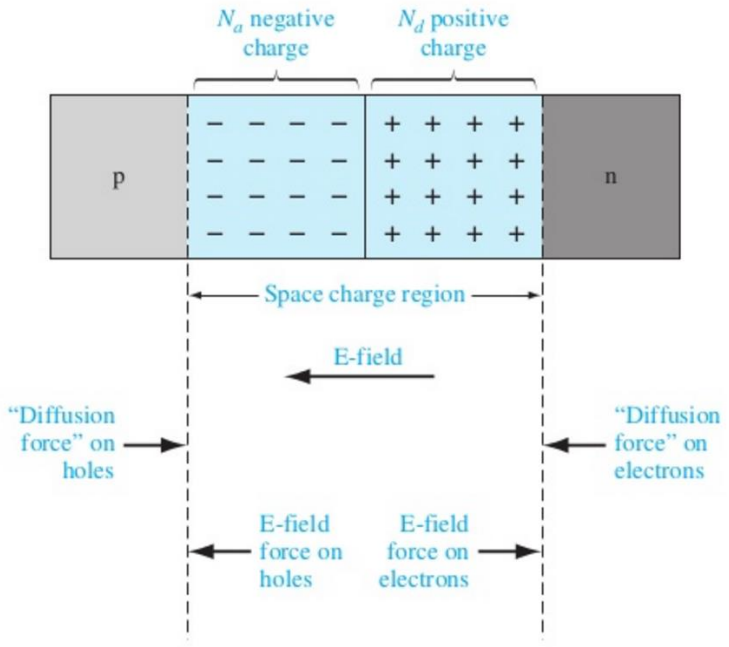

Figure 2: Depletion region, electric field, and forces acting on charged carrier with no external bias [6].

By applying an external bias to the p and n regions, the conditions for equilibrium no longer apply, meaning the Fermi energy level is no longer constant through the system. Figure 3 shows a p-n junction in the case of an applied reverse bias. The electric fields in the neutral p and n regions are negligible, which means that the magnitude of the depletion region's electric field must be higher than the thermal-equilibrium value due to the applied bias [6]. The number of positive and negative charges in the depletion region can only be increased if the depletion width, W, is increased; therefore, W increases with an increasing reverse bias, V_R [6].

With semiconductor detectors, incident radiation will pass through the depletion region, interacting and depositing energy. Ionization from this then creates electron-hole pairs. In the case of neutrons, reaction products are what create the electron-hole pairs, as neutrons are indirectly ionizing. An important factor when making a p-n heterojunction is the epitaxy between the two materials. Comparisons must be made between the atomic lattice constant for each material. Minimal lattice mismatch is required for proper function, with a mismatch of less than 5% needed. Fortunately, the lattice constant of high purity rhombohedral boron carbide has been measured. For boron carbide with carbon concentrations from 7.7-20.5 at%, Aselage et al. measured the lattice constant to be 5.62 Angstroms [7]. For (100) silicon, the lattice constant is 5.43 Angstroms [8]. Comparing these two lattice constants results in a lattice mismatch of approximately 3.5%, which is less than the required 5%. Because of this, (100) silicon is used as the substrate for the deposition of boron carbide.

Neutrons do not interact through Coulomb forces, making it more difficult to detect them than charged particles. Thermal neutron (~0.025 eV) detection generally relies upon nuclear reaction products that are generated from neutron captures. The reaction products deposit energy in the sensing medium, generating a measurable signal. For boron carbide, thermal neutrons are captured via ^{10}B, which has a neutron capture cross section of around 3800 barns. The possible reactions for this interaction can be seen in the following two reactions [5]:

$$^{10}_{5}B + {}^{1}_{0}n_{th} \rightarrow \begin{cases} {}^{7}_{3}Li + {}^{4}_{2}\alpha \ (Q - value: \ 2.792 \ MeV) \\ {}^{7}_{3}Li^{*} + {}^{4}_{2}\alpha \ (Q - value: 2.310 \ MeV) \end{cases}$$

This reaction results in the first excited state for the lithium ion 94% of the time, and it results in the ground state for the lithium ion 6% of the time. The resulting lithium and alpha ions can then ionize the detection medium, with the created electron-hole pairs collected at an anode and a cathode, creating a current pulse. This pulse can then be amplified and detected via signal processing equipment. Because a neutron needs to be captured and the reaction products need to deposit energy in the boron carbide, a thicker film will result in a higher detection efficiency.

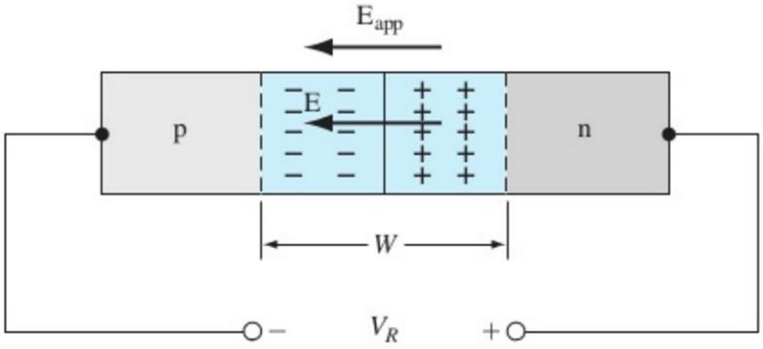

Figure 3: A p-n junction with applied reverse bias, V_R, and depletion width, W [6].

Researchers have investigated boron carbide conversion layer detectors for thermal neutron detection [9]. Because neutrons cannot be detected directly, a conversion layer detector utilizes a reactive material that has a large capture cross section for thermal neutrons. The reaction products generated then travel into the semiconductor material being used as the detector. Since the particles travel in opposite directions, only one of the particles can deposit its energy into the material per event. Unfortunately, the reaction products have a limited range, so if the film is made too thick, the reaction products may not make it to the detector material or may not have enough energy to generate electron-hole pairs. As a result of this, conversion layer detectors have a limited efficiency based on the range of the reaction products and the thickness of the film coating [10].

Stopping and Range of Ions in Matter (SRIM) was used to determine the range of the reaction products in boron carbide. By using the properties of B_4C, a range of approximately 1.69 μm was found for the ^{7}Li ion, and a range of approximately 3.34 μm was found for the ^{4}He ion. Conversion layers grown thicker than this would start to have reaction products not making it to the detection medium. If the boron carbide is instead used for both the capture of the neutron and the detection of the resulting signal, the thickness would not be limited to the range of the reaction products. In fact, increasing the thickness of the film to approximately 12 μm would allow for full charge collection of the generated electron-hole pairs, assuming a single-crystalline growth.

Chemical Vapor Deposition

Chemical vapor deposition (CVD) can be performed via several different methods, but in each case, it is a very complex process. It is the process of chemically reacting a volatile compound that is to be deposited with other gases to produce a nonvolatile solid, with this depositing atomistically on a suitable substrate [11]. It differs from physical vapor deposition (PVD), as it does not rely on material transfer from sputter target sources or condensed-phase evaporant [11]. Several different types of CVD techniques exist, each with advantages and disadvantages. These include, among others, low pressure CVD (LPCVD), plasma-enhanced CVD (PECVD), hot filament CVD (HFCVD), synchrotron radiation induced CVD, and atmospheric pressure CVD (APCVD). In addition to these techniques, CVD systems can be either cold-walled or hot-walled. No matter the CVD process, there are a set of fundamental sequential steps. Figure 4 shows most of these steps, as it represents a sequence of gas transport and reaction processes contributing to CVD film growth [11].

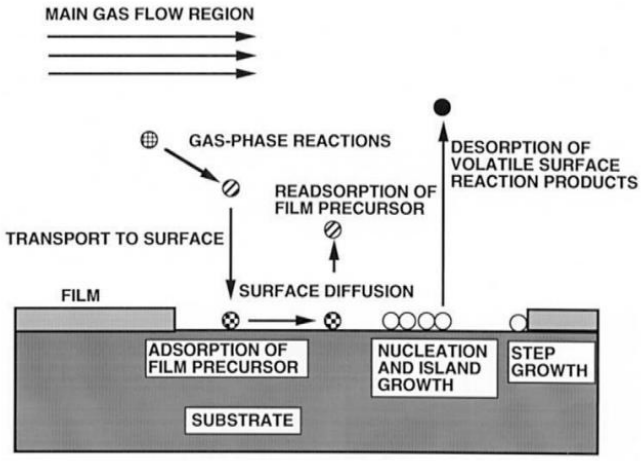

Figure 4: Typical sequence of gas transport and resulting reactions for CVD film growth [11].

Cold-walled CVD systems do not heat everything and focus only on heating the substrate. This may require active cooling of the chamber walls, depending on how the heating is accomplished. By only heating the substrate, a higher growth rate of films can occur than a hot-walled system, and there is likely less contamination than a hot-walled system. A hot-walled CVD system heats both the substrate and the chamber, typically via a surrounding furnace. This introduces an increased risk of contamination, as reactions could then occur between the chamber walls and the gases.

Beyond this, there are also different reaction types for CVD systems. Some of the possible reaction types are the following: pyrolysis, reduction, oxidation, compound formation, disproportionation, and reversible transfer. Pyrolysis reactions involve the thermal decomposition of hydrides, carbonyls, and organometallic compounds on hot substrates. An example of this is the low-temperature decomposition of nickel carbonyl to deposit nickel films [11]. Reduction reactions commonly employ hydrogen gas to impact the reduction of halides, carbonyl halides, oxyhalides, or other oxygen-containing compounds. An example of this is the reduction of silicon tetrachloride ($SiCl_4$) on single-crystal Si to produce epitaxial Si films [11].

CHAPTER TWO

LITERATURE REVIEW

Cold Wall CVD

Vandenbulcke et al. grew thin films of boron carbide in 1981, utilizing a cold-walled CVD system. Both continuous and homogeneous layers of boron carbides were deposited using a stagnation flow technique. The experimental setup can be seen in Figure 5 below, with Figure 6 showing the substrate and deposition surface in more detail. The B–C solids were deposited from a mixture of hydrogen (H_2), boron trichloride (BCl_3), and methane (CH_4). These gases were blown perpendicularly onto a flat disk of graphite that was heated by a radio frequency (RF) generator. In this experiment, H_2 was used as the carrier gas, while BCl_3 and CH_4 were both used as the reactant gases. The growth was performed at atmospheric pressure and a temperature range of 1127 to 1727°C, with a deposition time ranging from 30 seconds up to 10 minutes [12].

From the results of this growth setup, it can be seen that the deposition ratio of boron and carbon in the films is a function of the partial pressure of CH_4 and of the temperature of the system. A comparison between the calculated and experimental results, some of which can be seen in Figure 7 below, indicates that there is a fairly significant limiting effect stemming from the surface kinetics, as the experimental deposition rate is much lower than the theoretical rates and the solid composition differs from what was expected at equilibrium [12]. Figure 7 shows the theoretically- and experimentally-determined deposition rates of boron and carbon under these conditions: T=1527°C, partial pressure of BCl_3=0.2 atm, and mass flow rate of 0.04 g cm^{-2}-s^{-1}. As the graph shows, the deposition of boron carbide seems to be slightly limited by some sort of surface kinetic constraint—most likely from the inhibition of the kinetics by CH_4. It was found that the amount of departure from equilibrium increases with increasing mass flow rate and an increasing CH_4 partial pressure. A decrease in the temperature and a decrease in the BCl_3 partial pressure will also cause a departure from equilibrium. In addition, the kind of reactants employed, especially the carbon-containing species, can cause a departure from equilibrium. Figure 8 presents the deposition regions of the different boron and carbon structures as a function of temperature and of CH_4 partial pressure. At around 1627°C, which is near equilibrium conditions, the rhombohedral boron carbide phase starts to dominate, as it is the equilibrium phase encountered in the binary B–C phase diagram [12].

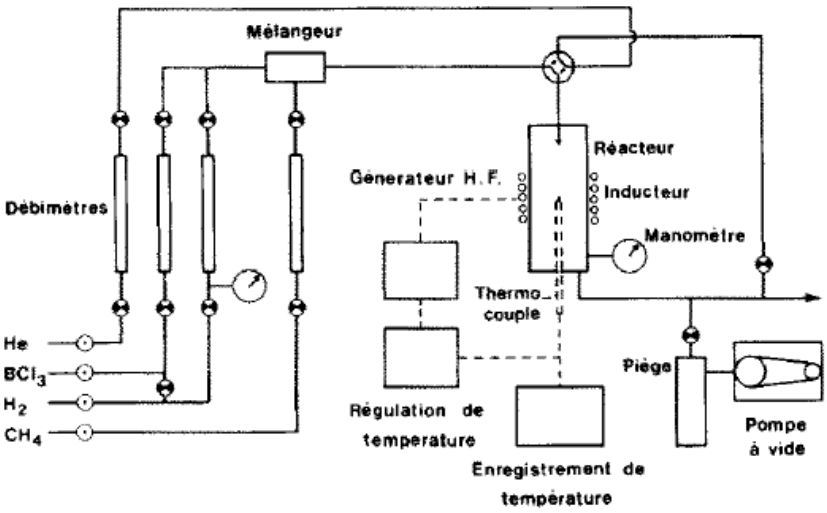

Figure 5: System setup for the cold-walled CVD growth process [12].

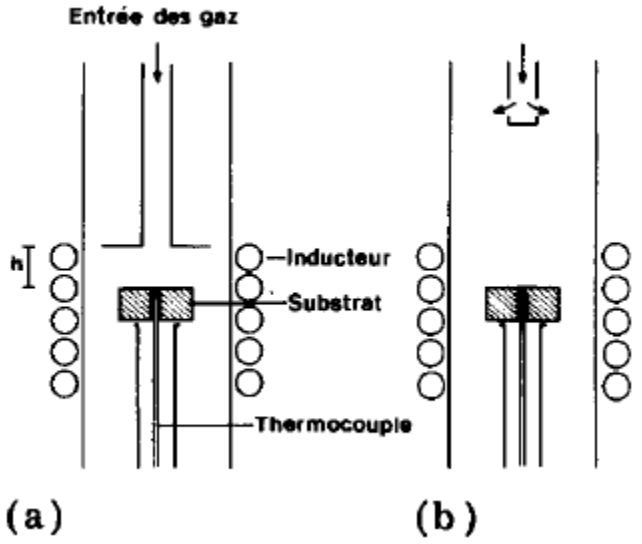

Figure 6: Internal view of CVD system [12].

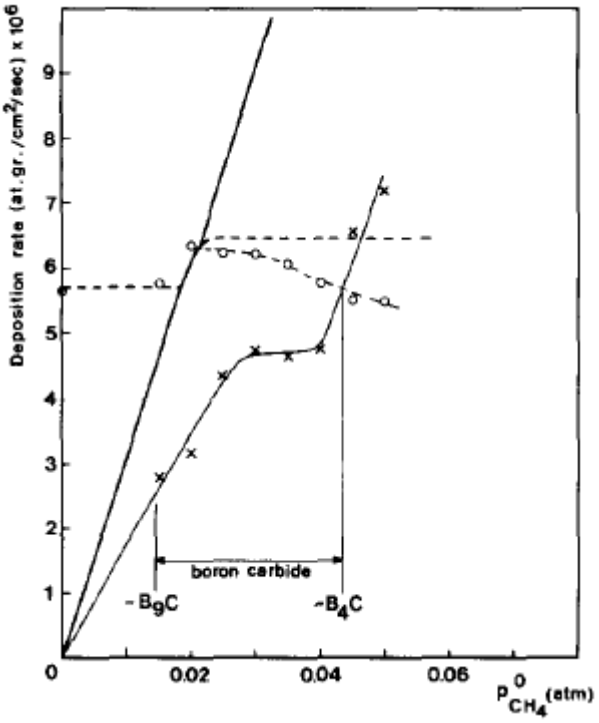

Figure 7: Theoretical and experimental deposition rates of boron and carbon at set conditions (T=1527°C, partial pressure of BCl_3=0.2 atm, and mass flow rate of 0.04 g cm^{-2}-sec^{-1} [12].

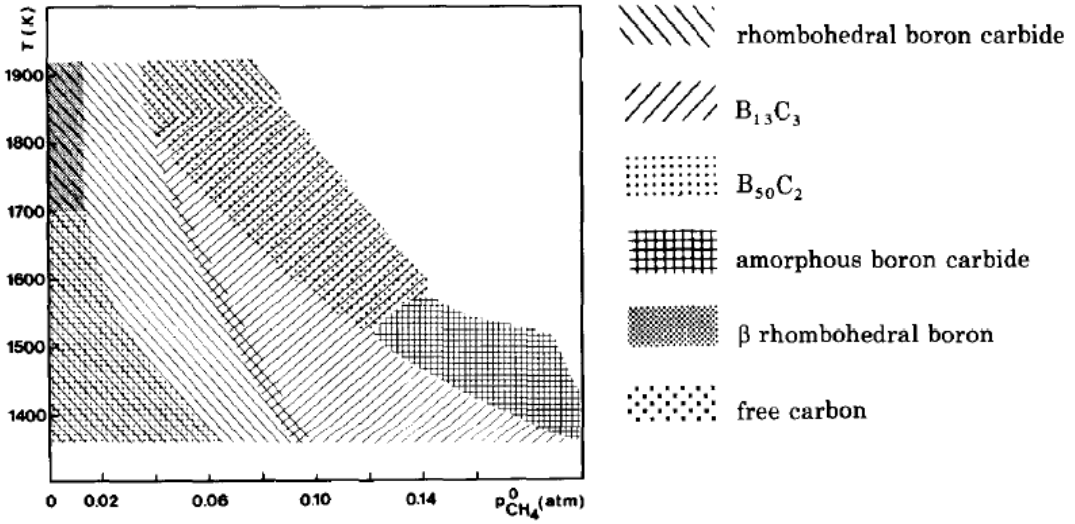

Figure 8: Deposition regions of the different boron and carbon structures as a function of temperature and of CH_4 partial pressure [12].

From this experiment, it appears that the composition, structure, and morphology of the binary B–C deposits depend on the temperature, amount of departure from equilibrium, and the interfacial conditions of deposition. Departure from equilibrium increases when temperature decreases, when the inlet molar fraction of BCl_3 decreases, when the inlet molar fraction of CH_4 increases, and when the mass flow rate increases. The B–C phase diagram phases are produced under near-equilibrium conditions, but other forms can often be obtained by CVD under kinetically-favored conditions of deposition when departure from equilibrium occurs [12].

Niihara et al. looked into the effects of stoichiometry on mechanical properties of CVD boron carbides in 1984. In particular, this study looked at the effect of the B/C ratio on the hardness and fracture toughness of B_4C. Plates of B_4C with thicknesses of 1 to 3 mm were prepared via CVD on a graphite substrate. BCl_3, H_2, and carbon tetrachloride (CCl_4) were used for the gases. The deposition time ranged from 1 to 4 hours for the experiment, with a deposition temperature of 1400-1900°C and a total gas pressure of 2.67-79.99 kN-m^{-2}. The flow rates for CCl_4, H_2, and BCl_3 were, in cm^3-min^{-1}, 80, 700, and 140-320, respectively [13].

Analysis of the plates shows that the B/C ratios varied from 3.65 to 5.88, depending on deposition temperature, total gas pressure, and flow-rate ratio of BCl_3 and CCl_4. It was found that B/C ratios of 4 to 5.8 consisted of single-phase B_4C of non-stoichiometric composition and the deposits with B/C ratios that were less than 4 consisted of B_4C and free carbon. The density of the compounds decreased rapidly with increasing C content for the B_4C and free carbon composites. In order to determine the fracture toughness, indentation tests were performed in a vacuum at loads of 0.98 to 9.80 N for 20 seconds. Clear radial cracks were formed under these conditions, with the crack length increasing with the load as $P^{3/2}$. This indicates the cracks on the surfaces correspond to the median cracks. Figure 9 below shows the fracture toughness and hardness of the various samples tested, with each data point representing an average of 5 to 10 indentations at an indenter load of 2.45 N for the fracture toughness. As is evident in the figures, both fracture toughness and hardness reach a maximum at essentially the stoichiometric composition B/C=4. It is likely that the decrease in hardness and fracture toughness with increasing B/C at B/C>4 is from the decreasing bond strength in the B_4C structure [13].

Kevill et al. grew boron carbide compounds via CVD in 1986. In this study, the B–C compounds were deposited by the flow of BCl_3 and CCl_4 in the presence of a large excess of hydrogen, with the surface maintained at around 997 to 1597°C. The general representation of the selection procedure used in this experiment can be seen in the below reaction [14]. Figure 10 shows the initial experimental setup used for this experiment; however, the system was then modified, replacing the RF generator by an Astro furnace and deposition was on a graphite liner situated in the hottest region of the tube. In addition, experiments were carried out where the graphite liner was replaced with a device that impedes flow of gases [14].

$$mCCl_4 + nBCl_3 \xrightarrow{excess\ H_2, 1000-1600℃} B_nC_m(+HCl)$$

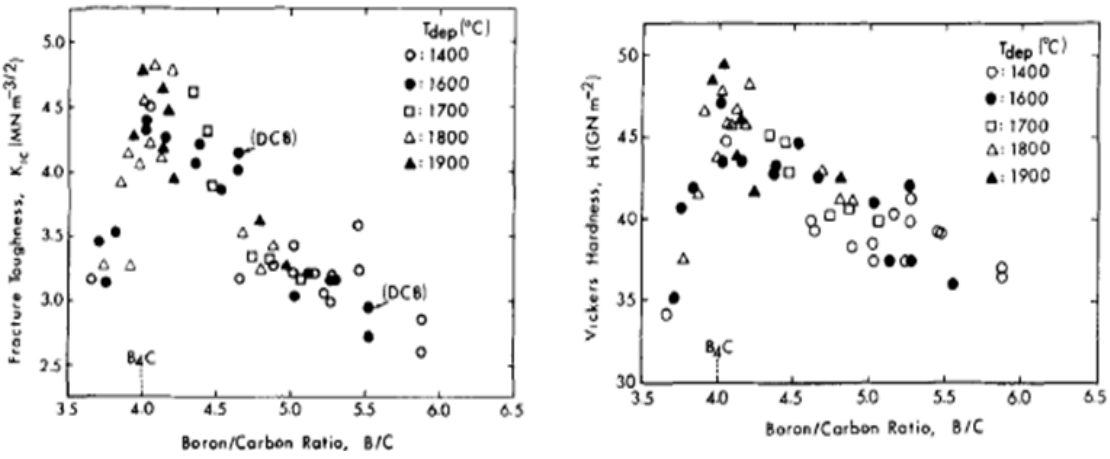

Figure 9: Fracture toughness as a function of B/C ratio (left) and Vickers hardness at 0.98-N load as a function of B/C ratio (right) [13].

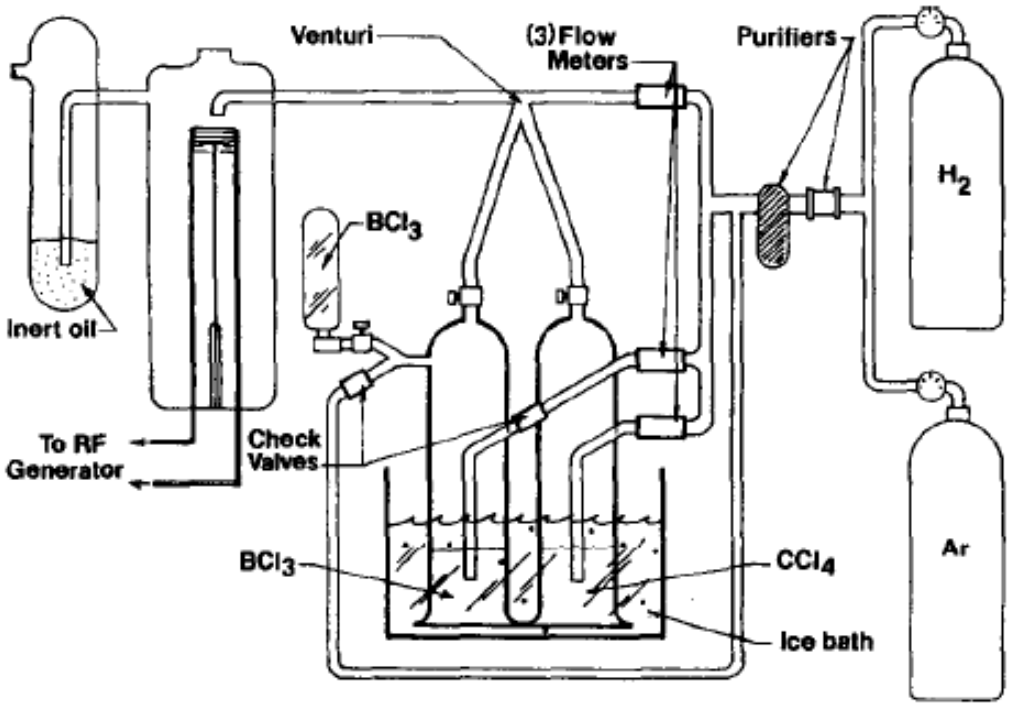

Figure 10: Experimental setup of the CVD system used to grow the boron carbide [14].

Initial growth results were found by varying the ratio of BCl_3 to CCl_4 to see the resulting composition. The deposition was performed on an RF-heated graphite disk. For deposit ratios of 4:1, 13:2, and 9:1 of BCl_3 to CCl_4 at 1250 to 1275°C, the carbon content came out to be around 22.1%, which lines up with the theoretical value of 21.7% in B_4C. This indicates that the composition of the material is independent of the molar ratio of BCl_3 to CCl_4. Deposition within a graphite tube was also explored in this experiment. A BCl_3 to CCl_4 ratio of 2:1, 4:1, 13:2, and 9:1 were all considered, with a BCl_3 plus CCl_4 flow rate of 0.05 g-min^{-1} in the presence of excess hydrogen. The depositions were carried out on a removable graphite liner inserted in a graphite tube that was heated in the Astro furnace. In this case, deposits at 2:1 and 4:1 ratios showed a uniform, dull-gray surface, while small crystallites could be seen in the 13:2 ratio deposit. Larger hexagonal plates were deposited in the 9:1 ratio, which resulted in a lower carbon content of 16.5% (i.e., $B_{5.62}C$, rather than B_4C) [14].

In 1986, Jansson et al. presented findings on the initial stages of growth of boron carbides from a BCl_3/H_2/hydrocarbon vapor on molybdenum. A low-pressure, cold-walled CVD system was used for this experiment. Thin foils of molybdenum (99.99% purity) were used as the substrates and were heated resistively, with a visual micro-optical pyrometer used for temperature monitoring. Any scratches on the foils were removed via electrolytic polishing. The deposition was performed at 1127°C, with a total pressure of 6.7 kPa and a gas-flow velocity of 15 cm/s. The partial pressure ratio between the boron trichloride and hydrogen was kept constant at 0.1 in all experiments [15].

The nucleation of boron on molybdenum was first investigated with a BCl_3/H_2 mixture. Boronizing of the substrate and formation of boron nuclei were both observed from this. The boron atoms initially diffused into the substrate with the formation of borides. After 15 seconds of deposition time, several borides with a total thickness of about 5 μm were observed in a cross section of the substrate. When CH_4 was added, boron carbides were deposited. It was found that the substrate could be boronized and/or carburized during the initial stages of growth. Small amounts of carbon were observed on the substrates that were exposed to the $BCl_3/H_2/CH_4$ gas mixtures after 10 seconds of deposition. These carbon concentrations were higher than when the substrates were exposed to BCl_3/H_2. The study then replaced CH_4 with C_2H_4. Again, the molybdenum substrates were boronized, but the boronizing rate was much lower than when methane was used. Only small amounts of carbon were observed in the substrates, and the surface of each substrate was completely smooth. These results show that the nucleation behavior of boron carbides on molybdenum is strongly influenced by the hydrocarbons used in the vapor, with increased concentrations of hydrocarbons reducing the boronizing and nucleation rates. The phase composition of the borides also seemed to be controlled by the concentration and type of the hydrocarbon in the vapor. With only a small amount of carbon being detected in the substrates, it seems that the strong influence of ethylene and methane on the initial stages of growth can be explained by the presence of adsorbed hydrocarbon fragments on the surface [15].

Jansson et al. grew thin films of boron carbide in 1989 via a cold-walled CVD system. The films were grown on a 5-10 μm thick α-rhombohedral boron substrate, and a BCl_3-CH_4-H_2 gas mixture was used for the deposition. Unlike some other studies that use this gas combination, this study was performed at a reduced pressure, rather than atmospheric pressure. The influence of experimental conditions on the phase and chemical composition of boron carbides formed at a reduced pressure (i.e., 6.7 kPa) was investigated in this experiment. While the H_2:BCl_3 molar ratio was kept constant at 10, other conditions were varied to observe the effect on the growth: the temperature ranged from 1027 to 1227°C, the pressure ranged from 1.3 to 6.7 kPa, and the CH_4 and BCl_3 vapor compositions were altered. The temperature range was determined because of a low deposition rate below 1027°C and because of poor adhesion above 1227°C. When altering the temperature, the pressure was kept constant at 6.7 kPa; when altering the pressure, the temperature was kept constant at 1127°C [16].

With this study, several metastable boron carbides were grown, with the carbon concentration ranging from 2% to about 7%. These different phases include $B_{13}C_2$, $B_{50}C_2$, $B_{49}C_3$, and $B_{51}C$. The rhombohedral phase, $B_{13}C_2$, had varying carbon concentration from about 7% to about 15% (compared to the generally accepted 9% to 20% for homogeneity), and it was deposited at higher CH_4 concentrations in the vapor. As these results show, a high carbon concentration was difficult to obtain using these experimental conditions. This could be fixed by increasing the total pressure or by increasing the deposition temperature. By using a hot-walled reactor, the experimental conditions used in this study could produce rhombohedral $B_{13}C_2$ with carbon contents closer to 20%. Figure 11 shows the influence of total pressure on the carbon content of $B_{13}C_2$. A decrease in total pressure results in a lower carbon concentration, with the lowest limit (1.3 kPa) resulting in deposition of the tetragonal T1 carbide [16].

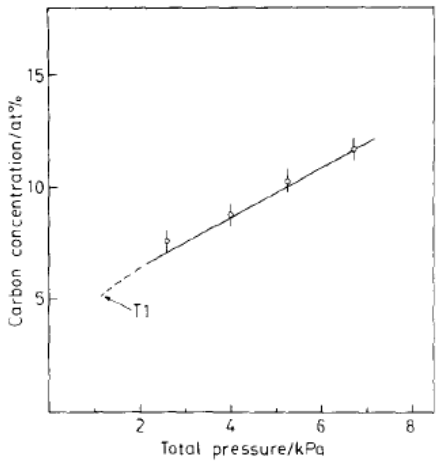

Figure 11: The influence of total pressure on the carbon content of $B_{13}C_2$ [16].

The experimental depositions obtained in this investigation have large differences from the calculated diagrams, as the calculated diagrams show that rhombohedral boron carbide is also formed for very small methane concentrations in the vapor; the calculations show that almost all methane in the vapor should react to form boron carbide or graphite. The experimental results show that rhombohedral boron carbide was difficult to grow, with low carbon concentrations being measured in the films that had high methane concentrations in the vapor. These results indicate that the deposition of boron carbide occurred far from equilibrium conditions, with the major reason likely being a kinetic barrier in the deposition of carbon [16].

In 2012, Chaudhari et al. utilized a hot wire chemical vapor deposition (HWCVD) technique using ortho-carborane as a precursor. A naturally occurring solid o-carborane was sublimated at ~70 to 90°C in a bubbler assembly designed especially for sublimation of o-carborane. In order to prevent condensation, the o-carborane vapor was carried into the reactor by argon gas through heated tubing. The boron carbide films were deposited to approximately 0.2 μm at 100 mTorr and a substrate temperature between 200 to 300°C, while the tantalum filament temperature was in the range of 1300 to 2000°C. This deposition was performed with only a rotary pump, rather than a turbomolecular and rotary pump combination. Infrared spectroscopy showed the presence of a prominent peak of a B–C bond at 100 cm^{-1}. Secondary ion mass spectrometry (SIMS) measurements have confirmed that there is ^{10}B in the film that was grown. The BC/c-Si heterostructure that was grown was subjected to forward and reverse I-V characteristics, as shown in Figure 12. These results show that a p-n junction was formed [17].

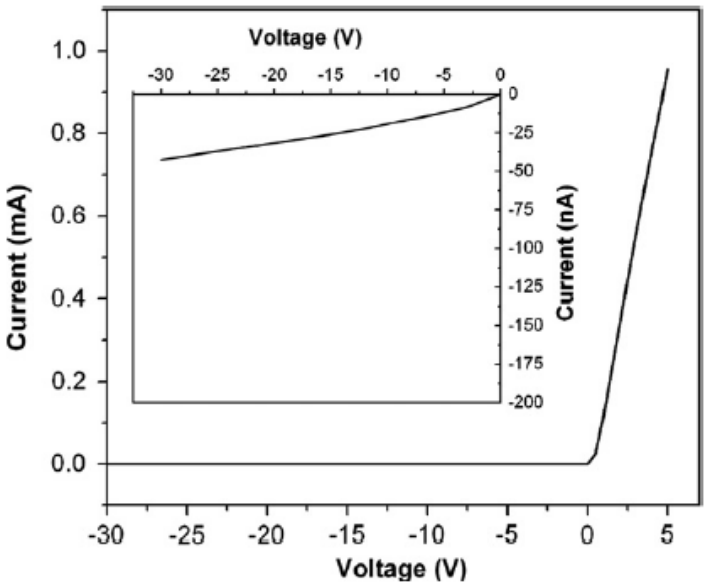

Figure 12: I-V measurements of the BC/c-Si heterostructure [17].

Plasma-Enhanced CVD

In 1992, Lee et al. studied the characterization of boron carbide thin films that were fabricated by PECVD from boranes. *Nido*-decaborane ($B_{10}H_{14}$) and *nido*-pentaborane (B_5H_9) were used for this experiment, along with methane. *Nido*-decaborane was found to be an air-stable, white crystalline solid and had a vapor pressure of several Torr at room temperature. The experiments were carried out in a custom-designed parallel plate 13.56 MHz radio-frequency PECVD reactor. Various boron carbide compositions were grown on n-type silicon and high-temperature glass. Unlike most of the other experiments discussed, a carrier gas was not used for these depositions. The deposition temperature, total pressure of reactants, applied power, and deposition time were fixed for each growth attempt. These were, respectively, 400°C, 50 mTorr, 20 W, and 30 minutes. The film compositions were determined via an Auger electron spectrometer equipped with a cylindrical mirror analyzer (CMA) [18].

For each deposition, the correct partial pressure for each mixture was attained and stabilized, with a plasma then created and held for the deposition process. It was found to be easy to grow pure boron carbide films, as long as the source compounds were pure or contained very little contaminants. When the films were exposed to air, oxygen was found, especially for the films fabricated from $B_{10}H_{14}$. In addition, the films grown with B_5H_9 seemed to be of a more uniform composition than the films grown with $B_{10}H_{14}$, which resulted in a larger investigation into the use of B_5H_9 for the growth of boron carbide films. Figure 13 below shows an Auger electron spectra for a typical film grown using B_5H_9 and CH_4, with little or no impurities found in the films. Analysis of the boron carbide films deposited on silicon showed that hydrogen is the only impurity in the source gases; however, the very thick films showed a hydrogen impurity level much less than 6% [18].

For this experiment, the partial pressure ratio was defined as the ratio of partial pressures for the source vapor pentaborane containing boron and the source vapor methane containing carbon [18]. Using this definition, a correlation between the partial pressure ratio and the boron-to-carbon ratio was found. Any systematic error in the experiment seems to have occurred from sample annealing temperature, plasma power, and total pressure. Even when available boron or carbon atom numbers are considered, it seems that the relationship between the partial pressure ratio and the boron-to-carbon ratio is not proportional. When using extreme partial pressure ratios (e.g., a drastic reduction or increase in B_5H_9 source particle pressure), only moderate film composition ratios are produced. This lack of proportionality suggests that there are many surface reactions that could be occurring, including carborane cluster formation initiated during the deposition process or gas phase plasma-initiated chemistry. X-ray diffraction (XRD) studies of the thicker films of boron carbide that were deposited on silicon exhibit boron carbide diffraction features, as seen in Figure 14. These diffraction lines range from $42° < 2\theta < 50°$ [18].

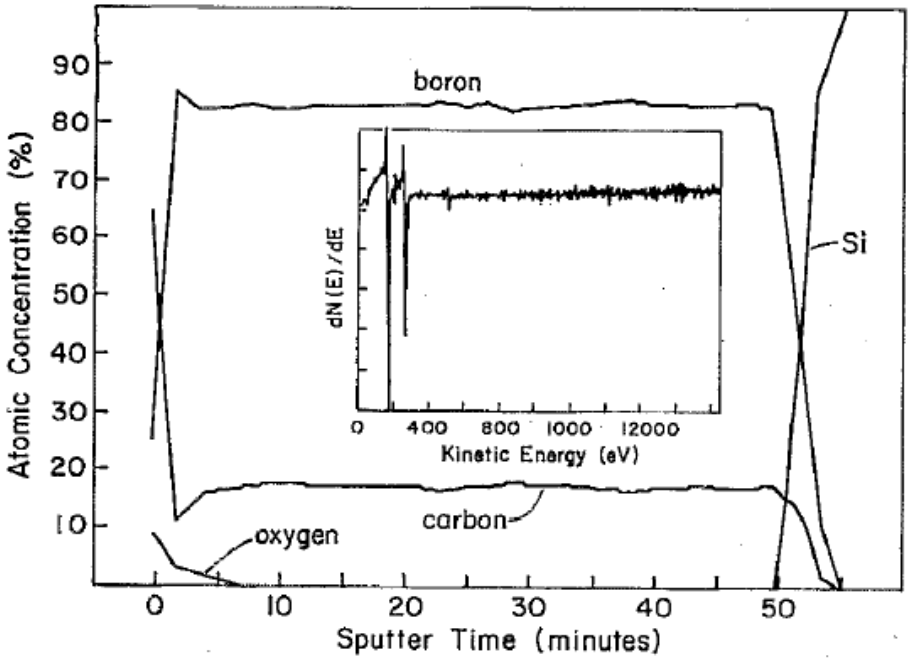

Figure 13: An Auger electron spectroscopy depth profile of boron, carbon, silicon, and oxygen of a boron carbide film that was grown from B_5H_9 and CH_4 [18].

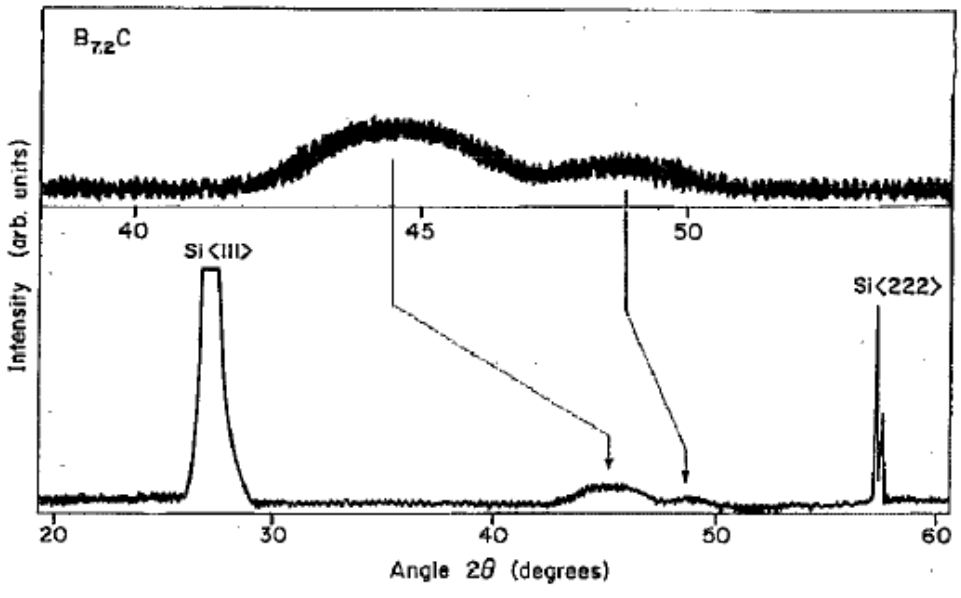

Figure 14: Broad peak of diffraction pattern for $B_{7.2}C$ from 20° to 60° in the 2θ range [18].

A wide composition range from 4.7 to 19.0 boron-to-carbon ratio at temperatures from room temperature to 100°C was looked at for the dark electrical conductivity. The conductivity seems to vary exponentially with the reciprocal of the temperature, whereas little variation is seen in the conductivity when changing composition, as seen in Figure 15. The samples were illuminated with visible light, with this not showing a drastic change in the conductivity, meaning the conductivity is generally insensitive to visible light. The conductivities found for the films grown ranged from ~10^{-4} to ~10^{-10} Ω^{-1}-cm^{-1}, which is very small, especially when compared to previously studied boron carbide conductivities. This is likely because there is little free carbon when growing boron carbide films with PECVD, B_5H_9, and CH_4. This claim of little free carbon being present is supported by the thermal activation barrier, as the magnitude of the conductivities measured is seen for other boron carbides at temperatures well below room temperature. The thermal activation barrier for this study is around 1.25 eV, with it being virtually independent of composition. Others have also found that the thermal activation barrier is independent of composition; however, their conductivities were much higher and thermal activation barriers much smaller. In fact, the values found in this study lined up more with pure boron, instead of boron carbides fabricated by other methodologies, which further supports the claim that there is little free carbon in this process of growing boron carbide [18].

The band gap of the films produced over the composition range of 2.4 to 50 boron-to-carbon ratio was measured. With the highest carbon concentration, the lowest band gap of 0.77 eV was obtained, while the band gap could get all the way up to 1.80 eV. Unlike the conductivity, it seems that the band gap is closely related to the composition of the boron carbide films grown—albeit this study finds that the band gap shows a greater dependence on composition than indicated by some other measurements. While the band gap for boron-rich films obtained in this study agree with some other studies (e.g., 1.5-1.6 eV and 1.6-2.0 eV), it is somewhat larger than other band gaps found (1.34 eV). When comparing the measured band gaps at room temperature with theoretical band gaps, they are generally smaller than expected, which could be from the fact that band gaps are calculated by density functional theory and that is often wrong for zinc blende and diamond structure semiconductors. In addition, boron carbide fabricated via PECVD could have a somewhat different structure than the one commonly fabricated, which could also account for differences in conductivity and band gap values [18].

In 1993, Lee et al. again looked into the structural homogeneity of boron carbide thin films fabricated using PECVD. Similar to the study presented in 1992, *nido*-pentaborane and methane were used to grow the films on silicon. The experimental setup was the same as the study the group did in 1992, with the deposition temperature again being around 400°C. The film compositions were controlled by adjusting the partial pressure ratio of B_5H_9 and CH_4. Varying film thicknesses (0.1 to 1.0 μm) were grown. The composition and thicknesses were again determined via Auger electron spectroscopy, as well as a profilometer [19].

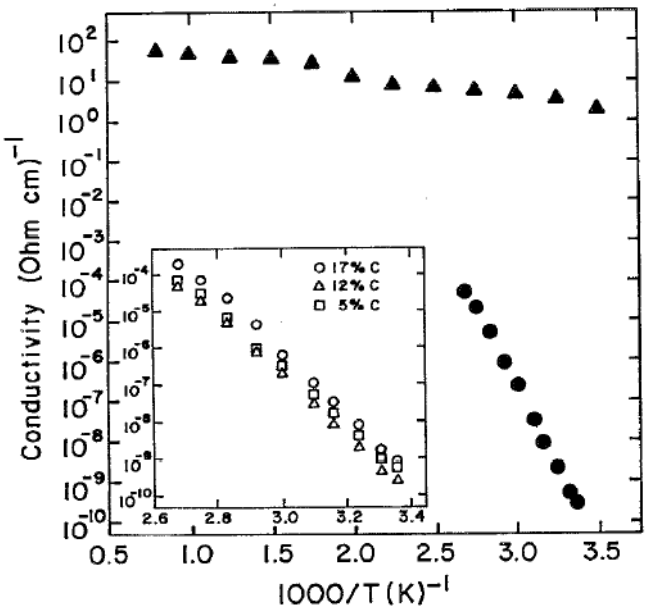

Figure 15: Boron carbide (approximately 20% carbon) sample conductivities vs. reciprocal temperature [18].

A wide range of stoichiometries (0.29<B/C<49) of boron carbide were obtained for the films grown in this experiment. As presented in the previous study, the film composition is not directly proportional to the composition of the reactant gases, likely from surface reactions including carborane cluster formation. The concentration of boron and carbon seemed to be very uniform throughout the films, with little impurities found, besides small amounts of hydrogen and sometimes oxygen, which again was found when introducing the films to air. A very low DC electrical conductivity suggests that the films grown are homogeneous and single-phase. The microstructure of the thin films was found to be the same as those presented in the previous study. The microstructure of boron carbide on silicon made via PECVD from diborane indicated an inclusion of hydrogen and helium, with a transition temperature in the range of 730-800°C between an amorphous and a microcrystalline structure [20, 21]. The films grown with B_5H_9 exhibit X-ray diffraction patterns more along the line of microcrystalline or polycrystalline boron carbide, with there being an indication of an amorphous film from the reflection high energy electron diffraction (RHEED) pattern [19].

Boron carbide grown via PECVD with B_5H_9 and CH_4 in this study appears compositionally homogeneous over a wide composition range, with microcrystalline films deposited onto a silicon surface at lower temperatures than other precursors. These boron carbide films that were grown seem to have a high resistivity, as there were no precipitates of carbon or other conductive phase [19]. Using PECVD to grow boron carbide seems to cause vastly reduced conductivities than boron carbide fabricated over other methods. It also shows a strong relationship between band gap and composition,

with increasing carbon concentrations reducing the band gap. This is consistent with models proposed by Werheit and co-workers [18]. It is possible that the reduced conductivity is from the lack of free carbon when compared to other fabrication techniques. The boron carbide films produced by PECVD demonstrated the capability of producing photosensitive p-n heterojunction diodes [19].

In 1992, Künzli et al. looked into the influence of B_2H_6/CH_4 and trimethylborane ($B(CH_3)_3$) as process gases on boron carbide coatings. They utilized an RF plasma-assisted chemical vapor deposition (PACVD) method in order to deposit the boron carbide. The process was performed in a high vacuum chamber at a base pressure of approximately $2.25*10^{-7}$ Torr after baking the chamber at a temperature of 100°C. The depositions were prepared at room temperature and were deposited on Si substrates. Before the depositions, the substrates were cleaned by Ar^+ ion bombardment, until no oxygen and carbon contamination could be detected. A few other typical deposition parameters are the following: self-bias voltage of -200 to -250 V, power of 300 to 400 W, total gas flow of 20 to 140 standard cubic centimeters per minute (sccm), and deposition time of 2 to 30 minutes [22].

The boron-to-carbon ratios in the process gas were chosen as 4:1, 1:2.5, and 1:3. Depositions with pure methane and pure B_2H_6/He were also used. $B(CH_3)_3$ was also used on different substrates (Au and Sn). When using different gas mixtures of B_2H_6/CH_4, an increasing growth rate was associated with increasing methane content in the process gas. Typical thicknesses when using B_2H_6 were in the range of 50 to 750 Angstroms. When using similar deposition parameters, other than gas flows, thicknesses of 1000 to 1200 Angstroms were obtained with $B(CH_3)_3$. The two different process gases produced similar electronic structures, but $B(CH_3)_3$ had a slightly higher growth rate. Oxygen contaminations were negligible in both cases, and all coatings showed good adherence to the substrate, with no peeling off observed after atmospheric exposure [22].

As a study in 1999, Zhang et al. looked into the growth and characterization of boron carbide nanowires via PECVD. The nanowires were grown on silicon substrates in a parallel plate PECVD chamber. The plasma power was kept at 50 W, and the temperature was between 1100-1200°C. Argon was used as the carrier gas and ortho-carborane ($C_2B_{10}H_{12}$) was used as the reactant gas. The argon flowed through the source bottle at a temperature of 50°C during deposition. The substrates were placed on the grounded electrode during deposition [23].

A thickness of ~1 μm was obtained after 2 hours of deposition using these experimental parameters. The boron carbide deposits appear to be a dull grayish-black color, and scanning electron microscopy (SEM) revealed that the deposits are highly porous, with an array of nanowires. The nanowires vary in diameter from roughly 18 to 150 nm and have lengths beyond 13 μm, which corresponds to aspect ratios ranging from 9 to 720. There were three forms of the nanowires present, with all present on an individual substrate: cylindrical with smooth surfaces and an average diameter of 20 nm,

cylindrical with rough, faceted surfaces and an average diameter of 50 nm, and linear arrays of roughly equally-spaced rhomboidal nanostructures. Selected-area diffraction (SAD) showed that the nanowires and rhomboidal structures are monocrystalline with a rhombohedral crystal structure. $B_{13}C_2$ has identical crystal structures and similar lattice parameters to B_4C, making it difficult to correctly identify the phase. Although the study could not unambiguously identify the B-C phase, energy dispersive spectroscopy (EDS) measurements indicated that the B:C ratio was close to 4:1, meaning the nanowires are likely B_4C [23].

The tips of the nanowires indicated the presence of iron, which had not been added to the growth chamber. This was likely the result of a contaminant present from a previous deposition. Because of the iron present in the tips of the nanowires, it is clear that they grew by the vapor-liquid-solid (VLS) mechanism, as this particular mechanism requires an impurity to act as a catalyst for crystal growth. The rough-walled nanowires may be smooth-walled nanowires with small boron carbide nanocrystals, based on their morphology. This would imply that the smooth-walled nanowires grow first, before acting as a nucleation site for further crystal growth. Because of the unique properties of boron carbide and the unique structure of these nanowires, it is possible that they could have unique quantum transport properties at low temperatures in a regime where polaronic transport is precluded [23].

Hot Wall CVD

Liu et al. performed low pressure chemical vapor deposition (LPCVD) to grow boron carbide in 2009. The boron carbide films were grown up to 18 μm thick onto 30mm x 15mm x 2mm graphite wafers. In this study, a BCl_3-CH_4-H_2 mixture was used and a low pressure chamber was used. Influences of deposition temperature, deposition time, inlet BCl_3/CH_4 gas ratio, and inlet H_2/CH_4 gas ratio on deposition rate and microstructure of the coatings were investigated in this study. The experimental setup can be seen in Figure 16; the deposition was performed via a vertical, hot-walled deposition furnace. The temperature within the reactor was calibrated by a thermocouple and the pressure was fixed at 10 kPa and measured via a pressure transducer [24].

Regression analysis was utilized in this study for both relative weight gain rate and average thickening rate against the deposition parameters in order to examine the influence of deposition parameters on deposition rate. This was accomplished with Uniform Design Version 2.20. From this analysis, it was found that the main factors affecting relative weight gain rate and average thickening rate are temperature, deposition time, and inlet BCl_3/CH_4 gas ratio. The equations produced from the software do not include the inlet H_2/CH_4 gas ratio, indicating that it could possibly be omitted in the effect on the CVD of B_4C for this study. From this analysis, it was found that the deposition rate varies most with temperature (varies exponentially), followed by the inlet BCl_3/CH_4 ratio (varies linearly), and then deposition time (varies linearly). Figure 17 shows the relationship between the relative weight gain rate and temperature for varying BCl_3/CH_4

gas ratios and varying deposition times. The optimized parameters for the maximizing average weight growth rate of B_4C were selected by the Uniform Design software as the following: temperature of 1100°C, a deposition time of 50 hours, an inlet BCl_3/CH_4 gas ratio of 5.0, and an inlet H_2/CH_4 gas ratio of 3.5. Results from the study showed that the deposited films were constituted by pyrogenation carbon (PyC) and B_4C at high temperatures (1050 to 1100°C). 1100°C and 1050°C resulted in an average boron content on the coatings of 49 and 45 at.%, respectively. When deposited at 900°C, the coatings displayed cluster surface morphology, with the microstructure and phase composition of the coatings homogeneous with a high boron content of approximately 79 at.% [24].

The results of these studies showed that B_4C coatings adhered to the substrates compactly and the thickness of the coating ranged from 0 to 18.0 μm. As previously mentioned, the major factors affecting deposition results are deposition temperature and inlet BCl_3/CH_4 gas ratio, with time having affected it slightly less and the inlet H_2/CH_4 gas ratio having little effect on the deposition rate. The different microstructure and phase composition coatings were deposited by three different kinds of mechanisms: the reaction products' nucleation mechanism (900°C), the polycyclic aromatic hydrocarbons nucleation mechanism (950°C), and the liquid phase nucleation mechanism (1050 to 1100°C) [24].

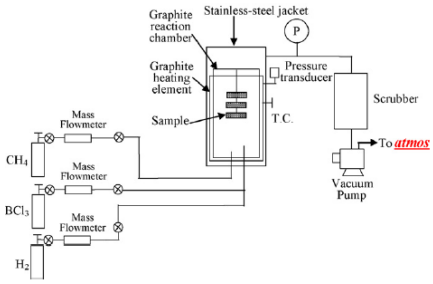

Figure 16: Experimental setup of hot-walled CVD system [24].

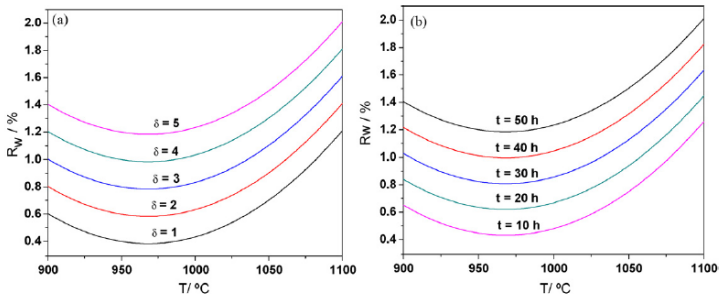

Figure 17: Relation curves between R_w and T. (a) Presents five inlet gas ratios at t=50 h and H_2 ratio=3.5. (b) Presents five deposition times at δ=5 and H_2 ratio=3.5 [24].

In 2011, Guan et al. investigated boron carbide nanowires using diborane and methane in a low-pressure CVD system via the vapor-liquid-solid growth mechanism. In this study, boron carbide 1D nanostructures were fabricated via co-pyrolysis of B_2H_6 and CH_4 at elevated temperatures on silicon wafers that have one micron thick, thermally-grown silicon dioxide. The substrates were cleaned and then coated with a 2-nm thick nickel thin film via magnetron sputtering. The substrates were then placed into a quartz boat and into a desired position in the quartz tube of the LPCVD system. A pressure of ~7 mTorr was used, with the temperature ramped up to 1050°C in 50 minutes. A constant argon flow of 15 sccm was used throughout the experiment, with 15 sccm B_2H_6 and 15 sccm CH_4 introduced to the quartz tube for 45 minutes at 1050°C and a pressure of ~440 mTorr. The subsequent substrates were analyzed via SEM [25].

Crystalline boron-based 1D nanostructures with various morphologies were fabricated because of unique combinations of temperature gradient and gas distribution in the system. $B_{50}C_2$ nano-ribbons were produced at 630-750°C. Tapered short boron carbide nanostructures approximately 2 μm in length were produced at 908-931°C. Long and thin boron carbide nanowires (~15 mm long) were found at 964-977°C. Figure 18 below shows an SEM image of as-synthesized nanowires, typical results for the crystallographic information of the nanowires as found via transmission electron microscopy (TEM), and EDS results showing the compositional information within the core, sheath, and catalyst of a nanowire. The nanowires have lengths up to 10 μm and diameters between 15 and 90 nm. Inset I in Figure 18b clearly reveals the catalytic material at the tip of the nanowire. The high-resolution TEM image of the black rectangle in inset I shows the nanowire has a single crystalline core, with a 0.5-2 nm thick amorphous sheath. The image reveals planar defects, such as twins and stacking faults in the nanowire. Inset II's streaks in the diffraction pattern further confirm the existence of planar defects. Based on the imaging in Figure 18b and 18c, the nanowire is found to have a rhombohedral boron carbide lattice. Because there are at least seven rhombohedral boron carbides (e.g., B_4C, $B_{10}C$, $B_{13}C_2$, etc.) with identical crystal structure and similar lattice parameters, it is difficult to distinguish phases between various boron carbides. Although it is difficult, this particular nanowire seems to have calculated lattice constants closer to $B_{13.7}C_{1.48}$, with a preferred growth direction being perpendicular to the $(101)_h$ plane. In this notation, h represents the hexagonal representation, and $(101)_h$ is equivalent to $(100)_r$, which is the rhombohedral representation [25].

Figure 18c shows the EDS results of the compositional information, with B, C, O, and Si all being found in both the core and the sheath. The Cu seen in the figure comes from the supporting copper grid and is not part of the nanowire. The higher O:B (or O:C) ratio observed from the sheath indicates that the nanowire's periphery is rich in oxygen. The atomic compositions shown in the five nanowires found in Figure 18c are semi-quantitative and are consistent with the fact that boron carbide has a varying carbon atomic percentage between 8.8 and 20%. The Si found in the core and sheath could have come from the substrates, quartz boats, or even the quartz tubes used for the growth [25].

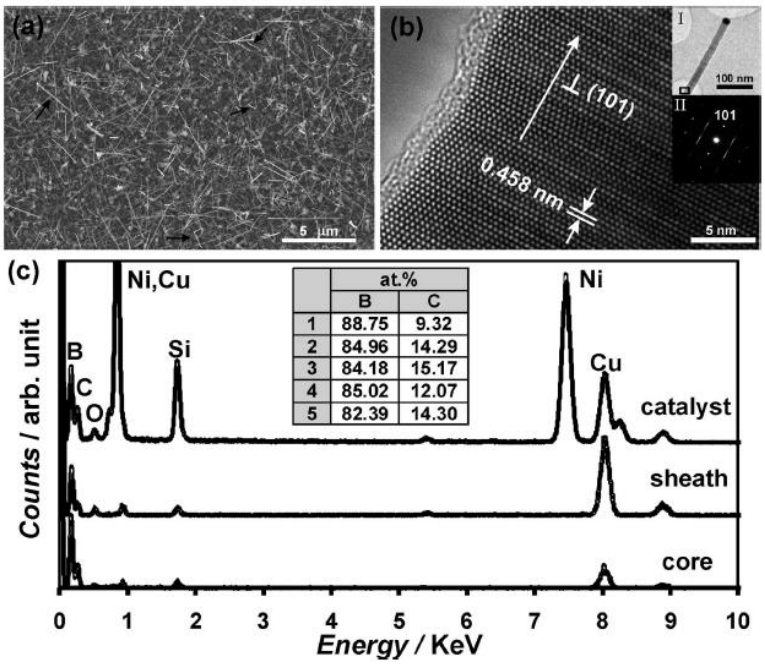

Figure 18: Materials characterization of as-synthesized nanowires, with (a) showing an SEM image of both straight and kinked nanowires, (b) showing TEM results and indicating a single crystalline core, and (c) showing EDS results for the compositional information within the core, sheath, and catalyst of a nanowire [25].

Various controlled synthesis experiments were carried out to investigate the growth mechanism and to optimize the growth conditions of boron carbide nanowires. The boron carbide nanowires only grew with the presence of catalytic materials, such as Ni. TEM analysis showed that Ni was commonly found at the tips of nanowires, indicating that the VLS mechanism was the method in which these nanowires grew. Leaving all other parameters constant, the reaction time was varied from 5 to 120 minutes. No nanowires were observed with a reaction time less than 15 minutes, while a reaction time between 15 and 80 minutes showed more and longer nanowires the longer the reaction time was. Increasing beyond 80 minutes did not result in more and longer nanowires; rather, it resulted in the coarsening of nanowires. An optimal reaction time of 80-90 minutes was found, which produced nanowires with a mean diameter of ~50 nm and an average length of 10 μm. The center temperature of the furnace was also varied from 900 to 1050°C in 50°C intervals. No nanowires were observed until the center temperature was at least 950°C, with this resulting in nanowires in the 879-885°C temperature zone region. Nanowires were found in the 964-977°C region with a center temperature of 1050°C. Higher center temperatures seem to lead to more and longer nanowires. The effect of the amount of gas precursors was also looked at, with nanowires growing with a ratio of flow rate between B_2H_6 and CH_4 of less than 5. A higher CH_4 flow also facilitated the growth of the nanowires [25].

This method of boron carbide synthesis seems to be more energy efficient than other widely used carbothermal methods, as it requires a much lower reaction temperature and shorter reaction time. The as-synthesized boron carbide nanowires were characterized as single crystalline boron carbide cores with thin amorphous oxide sheaths. Variable width twins and stacking faults were both observed as planar faults in the nanowires. The nanowires were grown via the VLS mechanism, but further investigation into the growth mechanism for the planar faults is needed. The thermal conductivities of these nanowires are significantly reduced values when compared to the reported thermal conductivities of bulk boron carbides. In addition, the thermal conductivity seems to have a dependence on diameter, with lower thermal conductivities being found with smaller diameter wires, suggesting that these nanowires could have significantly enhanced thermoelectric figures-of-merit compared to corresponding bulk boron carbides [25].

In 2013, Pallier et al. looked into the structure of amorphous boron carbide film in both an experimental and computational approach. The boron carbide ceramic was prepared via hot-walled CVD using BCl_3, CH_4, and H_2 at a deposition temperature of 1000°C. The optical band gap of B_xC films can be varied by changing the B/C ratio. Some benefits of boron carbide can be strongly limited by the poor oxidation resistance of boron carbide in air above 600°C; however, in the case of self-healing matrices, a high oxidability actually becomes an advantage, as boron carbide layers introduced in the last generation of silicon carbide-based composites are aimed at promoting matrix oxidation. This then forms a borosilicate glass, which seals the matrix cracks and protects the fiber reinforcement against oxidation; this particular feature provides self-healing matrix composites that have excellent durability under load in air [26].

The boron carbide coatings were obtained via a hot-walled CVD system with a deposition temperature of 1000°C and total pressure of 10 kPa. The system consists of a silica tube with a 100 mm inner diameter and is heated via an RF generator. The deposition area is ~100 mm long and can be approximated as quasi-isothermal (±5°C). The total gas rate was equal to 390 sccm and a deposition rate of ~1.5 μm/h was obtained. Most depositions were performed on open-cell vitreous carbon foams that have a pore size of 100 ppi, an apparent density of 0.05 g/cm^3, and a specific surface of ~55 cm^{-1}. Deposition times were typically around 6 hours, which led to thicknesses of ~9 μm. Before analyzing the samples, the foams were carefully crushed, and the carbon substrate was removed by oxidation in dry air at 430°C, with the a-B_xC ceramic then weighed and cleaned to ensure complete elimination of the original substrate. Once pure a-B_xC ceramic powder was obtained, the coatings were deposited onto silicon wafers. In addition, part of the a-B_xC powder was heat-treated for 2 hours at roughly 1300°C under a pure argon flow to allow for investigation of structural changes [26].

The composition of the films deposited were measured to be 70.5 at.% boron, 28.6 at.% carbon, and 0.9 at.% oxygen (i.e., a-$B_{2.5}C$), revealing a significant excess of carbon when compared to B_4C. Under the conditions of this experiment, it seems that the

equilibrium phase diagram suggests the existence of both rhombohedral B_4C and graphitic carbon. The density of the material is 2.47±0.01 g/cm^3, which agrees fairly well with the density of crystalline B_4C (2.52 g/cm^3). Figure 19 below shows that there are not any crystalline order or graphene sheets. A limited number of complete and diffuse rings can be seen in the inset of Figure 19, which is usually found for isotropic and amorphous material. The X-ray diffraction pattern and Raman spectrum both confirm the absence of crystalline boron carbide phases and pure carbon, unlike the thermodynamic predictions. Figure 20 shows the Raman spectra of the as-prepared (a-$B_{2.5}C$) and heat-treated (HT-B_xC) coating. The broad bands at ~400-700 cm^{-1} and 850-1350 cm^{-1} are typical of an amorphous state, while the more intense band centered around 1050 cm^{-1} could be from breathing modes of some icosahedron-like units. The absence of D and G bands that are characteristic of graphite-like carbon supports the claim that there is an absence of free carbon in the films [26].

There is a good agreement between the experimental and modeled structure factor and pair distribution function, as seen in Figure 21. All of the peaks found in the experimental functions are reproduced quite well in the model, both in terms of position and intensity. The model used atomistic $B_{154}C_{62}$, and the atomic structure and the reduced pair distribution functions for the experimental results were found via neutron diffraction [26]. The heat-treated material showed no change in the bulk chemical composition at the micrometer scale. An abundance of typical diffraction spots and lattice fringes were found, leading to the conclusion of rhombohedral B_4C being present in a highly crystalline state, which was confirmed by x-ray diffraction (XRD) analysis. The mean size of the B_4C crystallites, found via the Scherrer equation, comes out to be 44 nm. In addition, Figure 20 shows that free graphite-like carbon is clearly visible in the Raman spectrum, as the signal is dominated by the G and D carbon bands [26].

Figure 22 shows the pair distribution function of the heat-treated coating as obtained from neutron diffraction, with the modeled results also shown. Based on the model and experimental results, the as-deposited a-$B_{2.5}C$ coating contains a high amount of complete 12-atom boron-rich icosahedral units with compositions B_{12}, $B_{11}C$, or $B_{10}C_2$. Opposite of c-B_4C, the icosahedra are randomly located in an amorphous matrix, essentially consisting of sp^2 boron atoms and sp^3 carbon atoms. Clear signatures of tri-coordinated boron atoms were found in the amorphous materials, even though they did not seem to exist in the crystal. The heat treatment of the amorphous a-$B_{2.5}C$ coating allows for it to crystallize into rhombohedral boron carbide (B_4C). This crystallization is accompanied by free turbostratic carbon domains, as evidenced by Raman spectroscopy and TEM. As measured by neutron diffraction, two small peaks appeared in the probability density function (PDF) with the apparition of B_4C crystallites in HT-$B_{2.5}C$. Compared with the data from the B_4C model, the distances correspond to the C-B-C linear chains, confirming that linear chains do not exist in the amorphous state. The results of this study indicate that some carbon atoms from the amorphous state likely gain enough mobility to coalesce into free turbostratic carbon at elevated temperatures [26].

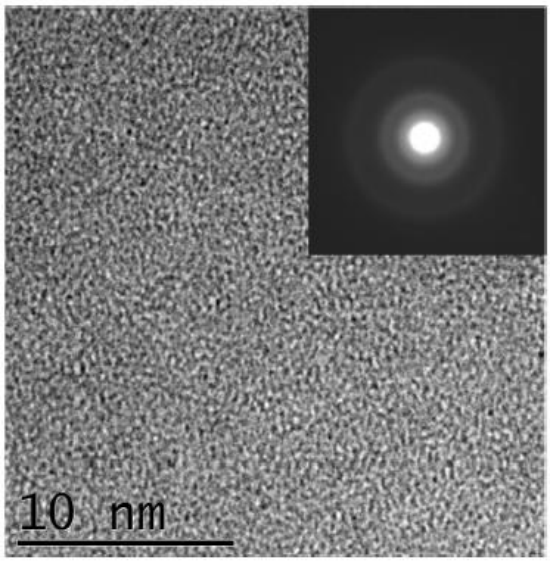

Figure 19: HRTEM image of a-$B_{2.5}C$ material, with SAED pattern shown in inset [26].

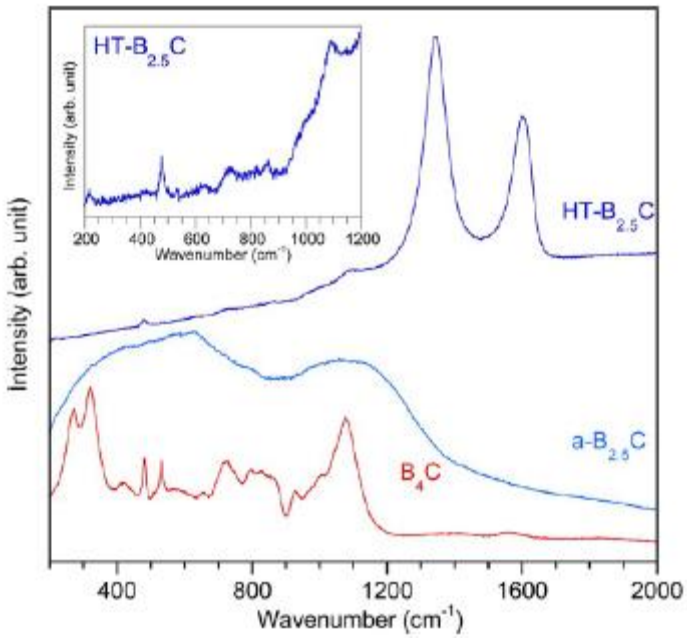

Figure 20: Raman spectra of the a-$B_{2.5}C$ and heat-treated coating, with the 200-1200 cm^{-1} region of the heat-treated spectrum highlighted in the inset [26].

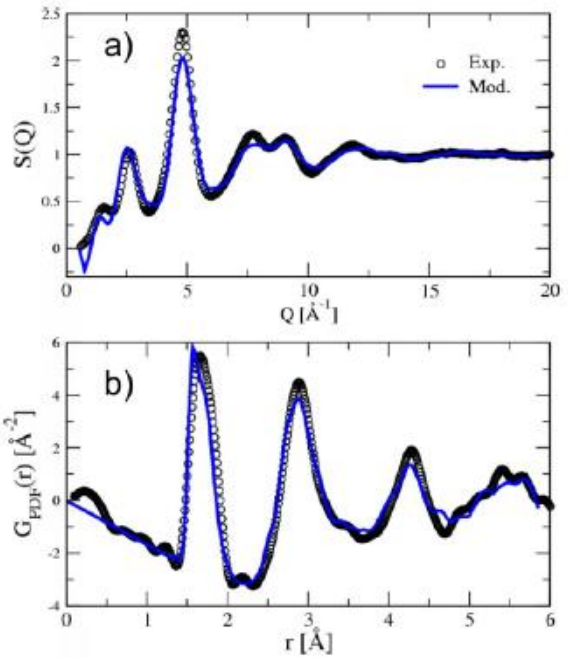

Figure 21: Structure factor (a) and pair distribution function (b) of amorphous boron carbide, with empty circles representing the neutron diffraction data obtained from the a-$B_{2.5}C$ material and the lines representing the $B_{154}C_{62}$ model [26].

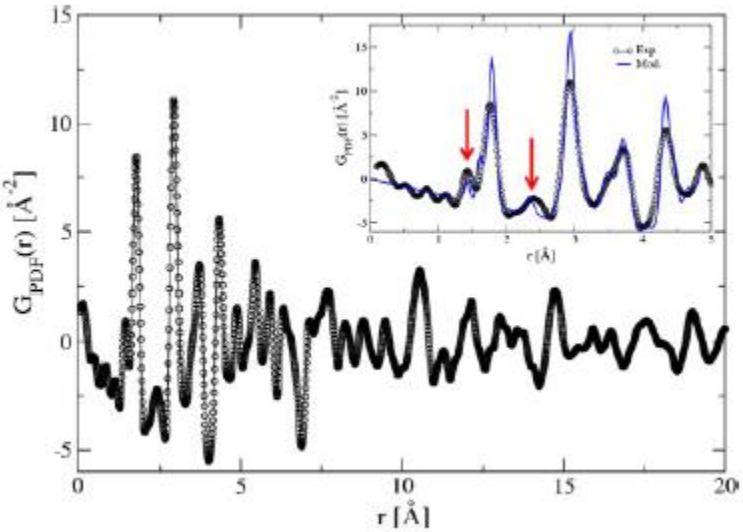

Figure 22: Pair distribution function of the heat-treated coating as obtained from neutron diffraction, with the inset showing the curve calculated from the model B_4C crystal [26].

CHAPTER THREE

DESIGN SELECTION AND EXPERIMENTAL METHODS

Gas Selection

Boron carbide thin films have been deposited with several different reactant gas combinations [12-19, 22-26]. A popular choice appears to be BCl_3 and CH_4 as the reactant gases, with H_2 as the carrier gas. Each study used different parameters (e.g., different temperature and pressures) and CVD processes (e.g., HFCVD and PECVD), so the resulting stoichiometry is different for each study. Studies have shown it is possible to grow B_4C with either BCl_3 or B_2H_6, along with CH_4 or CCl_4. Unfortunately, BCl_3 and B_2H_6 are both very dangerous. According to the Airgas Material Safety Data Sheet (MSDS) for BCl_3, it is a colorless gas with an obnoxious and sharp odor. It can cause serious eye damage, respiratory irritation, and severe skin burns [27]. According to the Airgas MSDS for B_2H_6, it is highly toxic. It can cause burns to the eyes and skin, and it is fatal if inhaled. It is a colorless gas, has a sickly sweet odor, and can ignite spontaneously in air [28]. With both gases being highly toxic, the choice was made to use B_2H_6 as one of the reactant gases. CH_4 is flammable, but it is less dangerous overall than CCl_4. Diborane also reacts with free chlorine, so CH_4 was selected as the other reactant gas. H_2 was selected as the carrier gas. When using B_2H_6 and a temperature of approximately 800°C, boron carbide can be deposited according to several published works [29, 30]

CVD System Design

In order to allow for fine control of the growth process, an HFCVD system was selected for the project. The system was designed and built with several different parts. Figure 23 shows a 3D representation of the early design for the system. The chamber for growth was selected as a base well and a bell jar. Since this system needs to be under vacuum conditions, the base well has to be connected to a vacuum pump. A table was custom-built in order to hold the system.

A stainless steel base well with an 11” inner diameter and eight ports from Huntington Vacuum was selected. The bell jar selected is also stainless steel and has two view ports, as well as a port on top, but it is unknown where it was purchased. Three Parker Model 201 mass flow controllers (MFCs) are used for the gases, with these each using Kalrez for seals because of its chemical corrosion resistance. These are controlled by a Parker Porter CM-400. Stainless steel tubing is used for all gas processes, except for the nitrogen flow to the vacuum pump. The system is put under vacuum via an Edwards iQDP80 Dry Semiconductor DryStar Vacuum Pump with iQMB-250 Booster purchased from spectraVAC. Attached to the exhaust of this pump is a NOVASAFE Dry Gas Abatement System. The table was built from aluminum extrusions and an aluminum plate. A pulley is mounted on top of the table, with a winch mounted to the table to allow

for the bell jar to be lifted up when needed. The gas tanks are all mounted to the side of the table, except for the B_2H_6 (1% in H_2) tank, as it is in a vented cabinet behind the table. Plastic is mounted all around the table to minimize the possibility of a gas leaking into the room without detection. Tungsten filaments are used to heat the substrate, with a 10 kW Lambda GEN 20-500 Power Supply used for the heating. Phosphorus-doped silicon wafers were selected as the growth substrate, with these being n-type and having an orientation of (100). Some of the wafers have a resistivity of 1-10 Ω-cm, with others having a resistivity of >10,000 Ω-cm. These substrates are placed onto a boron nitride plate, as boron nitride has high thermal conductivity and high electrical resistance. Additionally, it is chemically inert, non-toxic, and easily machined.

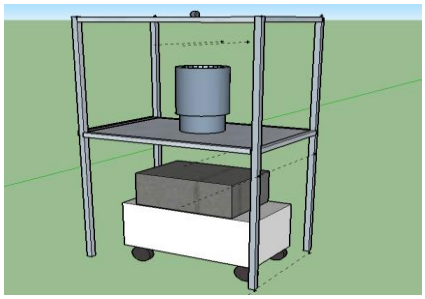

Figure 23: 3D representation of the initial design of the system.

System Construction

Before the system could be used, many things had to be considered. Most importantly, the correct base well needed to be purchased to make a good seal with the bell jar. Because the bell jar has an outer diameter of just under 13", a base well with an outer diameter of 12.875" was selected. Eight viewports were selected because several components would need to be fed through to the inner chamber. The Edwards iQDP80 with iQMB-250 was selected as the pump, so the base well also needed to have an ISO63 bolt flange on its bottom port to allow for connection to the pump. Figure 24 shows the base well with only the gas lines and high voltage lines in the chamber.

Because the bell jar was purchased before starting this project, its composition is unknown. With diborane, aluminum needs to be avoided, so verification that the bell jar is not aluminum was required. This was done via a scratch test and estimations of its density. Attempting to scratch the bell jar with a piece of stainless steel produced no visible signs of scratching. The density was calculated by weighing the bell jar and estimating its volume. The bell jar came out to be approximately 31.8 kg, and its volume was estimated to be 0.00468 m^3. The volume was estimated by assuming a thin-walled cylinder and adding in the view port areas as more thin-walled cylinders. By dividing the mass by the volume, the density comes out to be approximately 6795 kg/m^3. While this is lower than the density of stainless steel (~8000 kg/m^3), it is entirely too high to be

aluminum; therefore, the scratch test and density estimation provided enough evidence that the bell jar is stainless steel.

Figure 24: Base well without components placed in it.

After figuring out the base well and pump to be used, something was needed to actually hold the base well and bell jar up. Because the base well would need to connect to the pump somehow, an aluminum plate with a hole in the middle was selected as the table top. Aluminum extrusions were then selected for the frame of the system, as they are easy to machine and relatively cost effective. After some preliminary sketches and ideas, Bertelkamp Automation was contacted to verify that this design would work. They verified that the table should hold and provided a rendering of the table, as seen in Figure 25. The basic idea of the table is to mount the aluminum plate to the extrusions, place the base well through the hole of the table top, place the bell jar on top of the base well, place the pump underneath the table, and mount a pulley on the extrusion in the middle of the frame at the top. Careful measurements needed to be made for the table requirements because of space concerns, as well as the pump being a specific height and the base well having a specific diameter for its bottom port.

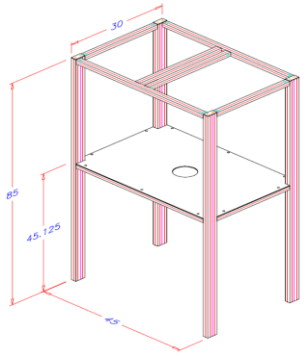

Figure 25: Rendering of table used to hold system, courtesy of Bertelkamp Automation.

To create the table, the aluminum extrusions were cut down to the proper lengths via a bandsaw. The extrusions for the table top are connected via connections from McMaster Carr that require no tapping, drilling, or counterboring. The connections screw into the extrusions with an Allen wrench and lock into place via a rotatable head. The extrusions at the top of the frame are connected via 3-way corner connectors, which does require tapping. Leveling feet are also used for the frame and to make the table even, with this requiring more tapping. Once the frame was all connected and set up, it would sway from very little movement. Although none of the weight was on it yet, as the table top, base well, and bell jar were not in place yet, the table swayed too much; therefore, support frames were added halfway between the table top and the top of the frame. These made the table much more stable. The aluminum plate purchased did not have a hole in the center, so it was cut out with a 6" diameter hole saw. The corners of the plate were cut to allow for the plate to fit on the frame. Figure 26 shows the frame without anything attached to it before adding the support to prevent the swaying.

Unfortunately, as Figure 26 shows, the table top was placed a little too high up, making it to where the pump and base well could not be directly attached to each other. A gate valve is attached to the top of the pump to help manage gas usage, and a custom stainless steel ISO63 nipple was ordered from Huntington Vacuum to allow for the base well and the pump to be connected without having to modify the table. Figure 27 shows the pump, gate valve, nipple, and base well all attached. Because the gas used is highly toxic, a dry gas abatement system is attached to the exhaust of the pump, to strip away as much as possible. The exhaust line then goes from there to the room exhaust. With the pump and base well connected, the pulley and winch were mounted to allow for the bell jar to be lifted when needed. The pulley was mounted on the bottom of the extrusion at the top of the frame, and the winch was mounted to the side of the aluminum plate. The rope attached to the pulley and winch is fed through the bell jar via two hooks that are attached to two eye bolts on the blank stainless steel flange at the top. Figure 28 shows the bell jar lifted from the base well, with the winch locked.

For each gas tank, stainless steel tubing is used. Nitrogen is used for the pump and for purging. A Swagelok union cross is used to split the nitrogen three ways. It is fed into the chamber via a gas feedthrough, with a quarter-turn valve used to close the line off when the chamber is not being purged. It is sent to the pump via plastic tubing, as this line is completely separate from the rest of the system. It is also sent through an SMC filter regulator and check valve to help with the safety of the diborane. The methane and hydrogen are fed into a Swagelok union tee, with the two mixing and going into the chamber via a gas feedthrough. A quarter-turn valve is used on the hydrogen line before the union tee to prevent any methane from flowing over to it during the carburization process. The diborane line is completely separate from the other gases until going into the chamber via another gas feedthrough. Once into the chamber, the two feedthrough lines go through a Swagelok union tee to completely mix the three gases before feeding into a custom-designed showerhead. Figure 29 shows the gas lines before going into the chamber.

Figure 26: Image of frame and pump without anything attached and without added support frames.

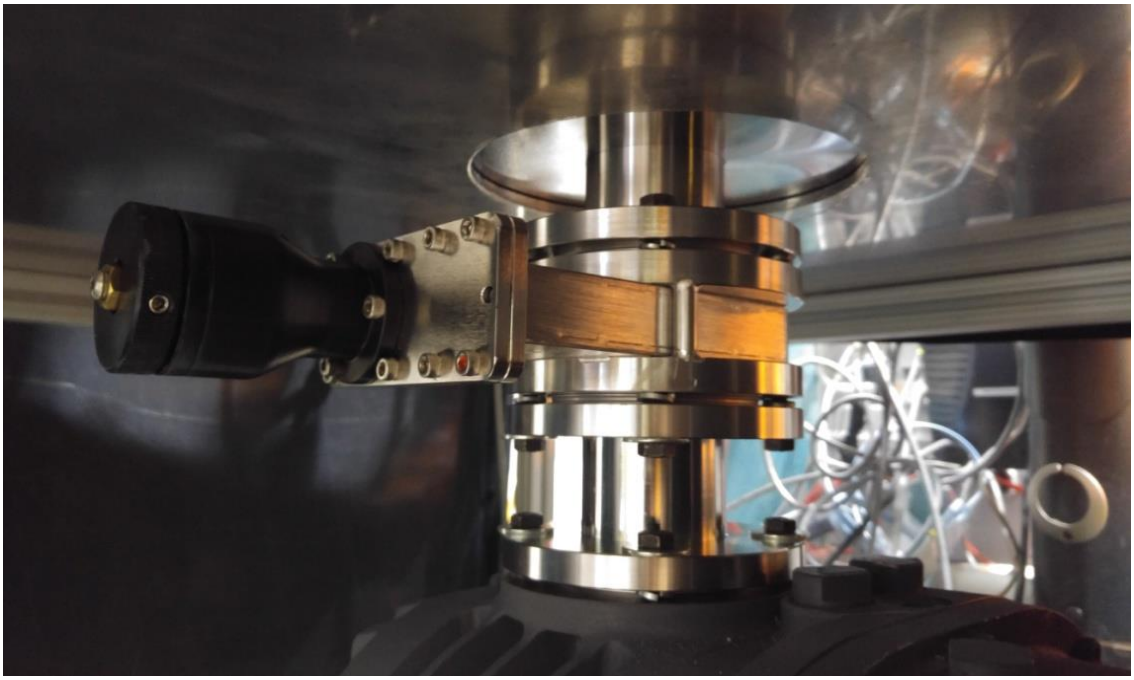

Figure 27: Pump, ISO nipple, gate valve, and base well all connected together.

Figure 28: System with the bell jar lifted off of the base well via the winch and pulley.

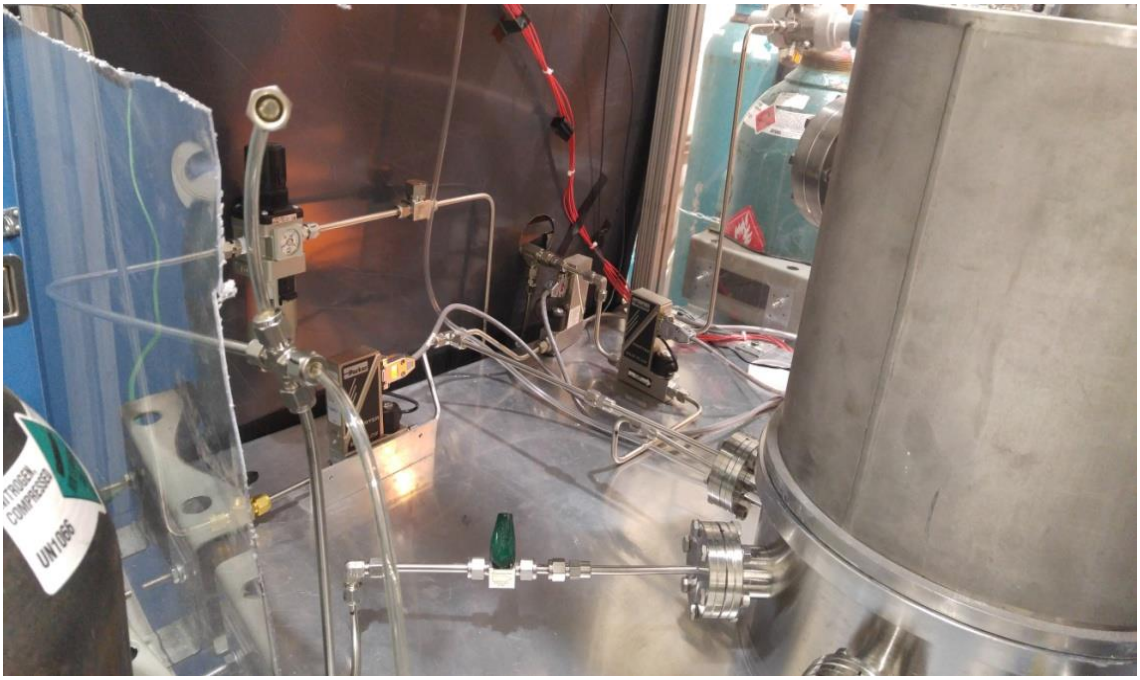

Figure 29: Gas lines before getting into the chamber (with the nitrogen disconnected from changing tanks).

Inside the chamber is a stainless steel mesh disc to prevent any debris from falling into the pump. A stainless steel table was built and welded to allow for the heating of the tungsten filaments used. Boron nitride blocks were machined and placed on this table, with machined copper bars being placed down into them. These copper bars have the tungsten filaments fed through them. The filaments are tightened on one end via set screws and allowed to freely expand and contract on the other end to accommodate for thermal expansion and extend the life of the filaments. These filaments are also carburized before growth to allow for a cleaner deposition. A stainless steel scissor lift is used to hold the silicon substrate. A thin boron nitride plate is placed on top of the scissor lift because of its high thermal conductivity. Another stainless steel table was built and welded to hold the showerhead. This table was initially too big for the chamber, so each leg was grinded down to allow for it to fit. Figure 30 shows the two tables and the scissor lift in the chamber without the boron nitride, copper bars, and showerhead—albeit the table holding the showerhead was altered to allow for the showerhead to be held in a more efficient way.

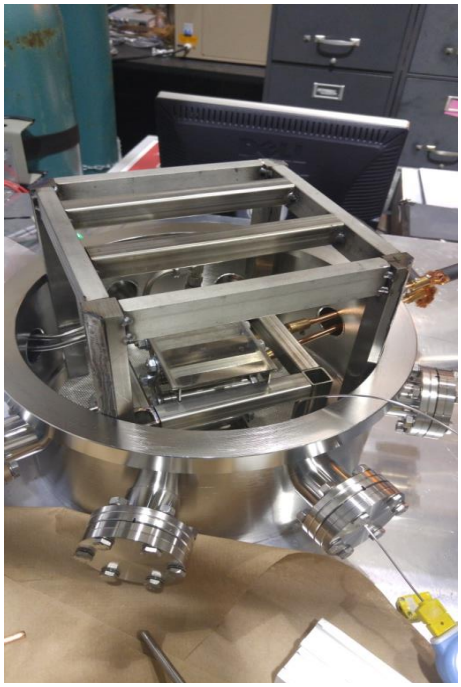

Figure 30: Initial design of the tables.

The gas needed to be delivered via some sort of showerhead. It was difficult to find a showerhead readily available for purchase, so a custom showerhead was designed and built. A thin-walled stainless steel cylinder was cut, with a stainless steel disc placed on the back side. The stainless steel disc has a hole in the center for the gas tubing. The side for the gas delivery has a boron nitride disc attached to it to try and prevent risk from

any type of arcing from the copper bars or tungsten filaments. This disc was cut out using a hole saw, and the disc was placed onto a mini drill press to create the holes in it for gas delivery. Holes were tapped in the stainless steel to attach the boron nitride, with ceramic screws used because of the possibility of electrical arcing. Figure 31 shows the showerhead in place on the table; however, this is with the initial design. The problem with this design is that the gases could have deposited onto the stainless steel cross bars. The redesign can be seen in Figure 32. For this, a single thin-walled stainless steel bar was welded to the table, and a bandsaw was used to cut into the bar on the end. The showerhead was then placed into the bar via a hose clamp. Because of how the showerhead is placed, there should not be any risk of deposition on the table.

The power supply used for heating the tungsten filaments is a Lambda GEN 20-500 Power Supply. This power supply can go up to 20 V and 500 A for a total of 10 kW. This power supply was selected because a high substrate temperature is needed for deposition. The tungsten filaments were selected with a 0.020" diameter, with the voltage and current needs verified via calculations. This was determined by assuming Ohm's Law applies to the system. Although this is not necessarily true, it gives an idea of what is needed. Because resistivity is a function of temperature, the resistivity of the tungsten was taken as 66 μΩ-cm, which corresponds to a temperature of 2000°C [31]. Nine filaments are used in the system, with the total resistance of the filaments coming out to be 0.11 Ω. Each filament is 6" in length. By using the maximum power output of the power supply and this calculated resistance, the current comes out to around 425 A. This results in a voltage of approximately 23 V. While this indicates that the power supply will not be able to allow full energy deposition in the wires, this shows that the 10 kW power supply should be sufficient for the heating done for the growth.

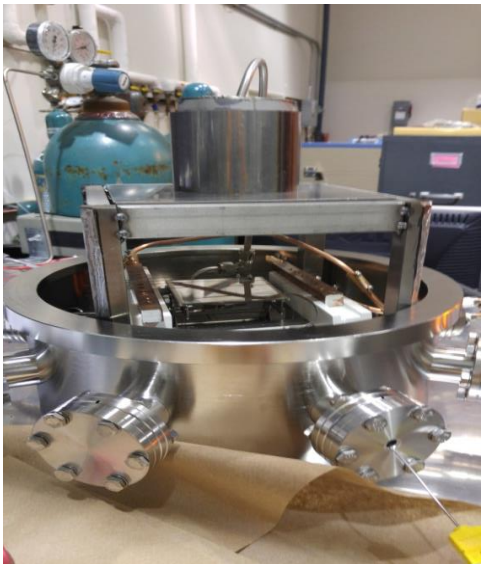

Figure 31: Table with showerhead (initial design).

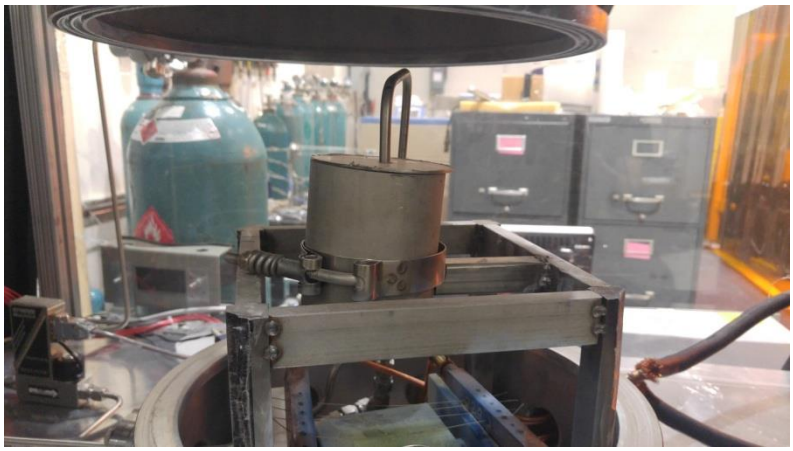

Figure 32: Redesigned table for showerhead with hose clamp and single bar to hold showerhead.

Diborane Safety

With how dangerous diborane is, safety was top priority when designing and building this system. Diborane is a boron hydride compound. At room temperature, it is a colorless gas, and its odor has been described in several different ways, including unpleasant, distinctive, and sickly sweet [28, 32]. While it is insensitive to mechanical shock, diborane is very toxic and decomposes slowly to hydrogen and higher-molecular-weight boron hydrides at room temperature [32]. Diborane is extremely flammable and has a high chemical reactivity. It can ignite spontaneously in air and is completely hydrolyzed by water. Additionally, it readily reacts with halogens, reactive metals, various inorganic compounds, and many organic chemicals [32]. In the case of a fire from diborane, the fire should be kept under control by water fog, but it should not be completely extinguished if it can be controlled, unless the source of diborane is depleted [28, 32-34]. This is because an explosive diborane-air mixture might accumulate if the fire is extinguished [32].

Like all boron hydrides, diborane is thermodynamically unstable at room temperature. At around 100°C, thermal decomposition becomes pronounced, with hydrogen evolved and condensed higher boron hydrides formed; these decompose at progressively higher temperatures to give elemental boron at around 600°C to 700°C [32]. If diborane burns in air, it creates a characteristic green flame, which gives off boric oxide and water (or boric acid) [32].

As previously mentioned, diborane is rapidly and completely hydrolyzed by water, which generates a lot of hydrogen gas. Reactions of diborane with halogens and hydrogen halides lead to terminal substitution and the formation of boron trihalides. Free chlorine is the most reactive agent from the halogens [32]. Boranes are electron-deficient, so they will accept electrons from active metals under suitable reaction conditions,

leading to borohydrides. Diborane is a selective reducing agent, reducing aldehydes, ketones, nitriles, esters, and other types of compounds [32].

Potential hazards involved with diborane are associated with three of the general health categories: toxicity (physiological activity), flammability, and explosivity. Since diborane is a highly toxic chemical, serious personnel health hazards can result from inhalation. Diborane is primarily a pulmonary irritant; inhalation of diborane vapors produces an exothermic reaction in the lungs as the borane is rapidly hydrolyzed to boric acid and hydrogen [32]. Severe exposure could impair the central nervous system, possibly by blocking the oxygen-reduction enzymes. The threshold limit used for diborane has been established as 0.1 ppm by volume, which represents the average concentration over a normal work day to which the average human can be safely exposed on a daily basis with no adverse effects. The odor of diborane offers some warning, but small concentrations may be below the threshold limit for detection by the nose. In addition to this, prolonged exposure to small concentrations of diborane may also temporarily impair the sense of smell, so odor should not be relied upon as a detection method [32].

Depending on the concentration inhaled, diborane can cause coughing, a sense of tightness in the chest, nausea, temporary elevated pulse, blood pressure, and temperature, fatigue, heaviness of legs, headache, and skeletal muscular tremors and spasms [32-34]. A person who has inhaled diborane may be slow to respond to questions, be dull, and have body movements not unlike mild alcohol intoxication. Patients may also lose control of a particular muscular function, such as the inability to hold up the head or to retract the tongue. Although diborane is highly toxic and hospitalization has been required for numerous cases, it should be noted that most reported exposures have caused only minor distress, which is likely from the fact that workers quickly leave the contaminated area once diborane is smelled or symptoms are noticed [28]. Diborane may cause damage to the following organs: lungs, liver, mucous membranes, kidneys, upper respiratory tract, skin, eyes, and central nervous system [28].

When using diborane, materials in contact with the gas are very important, as diborane will react with many materials. All materials in contact need to be thoroughly cleaned. Stainless steel and low carbon steels are unaffected by diborane, but rusty iron causes the decomposition of diborane at atmospheric pressure [32]. Investigations found that most common metals are safe for use with diborane; however, their oxides are not. Most rubbers and other nonmetallic materials are attacked by diborane, meaning that care must be exercised in the selection of seals, gaskets, lubricants, solvents, etc. [32]. Of particular note, aluminum is incompatible with diborane, while stainless steel, copper, tungsten, boron nitride, Kalrez, PTFE, Pyrex, Quarts, Teflon, and Viton are all compatible.

With all of this in mind, the safety features of the system were considered. Each material to be in contact with the diborane was checked for compatibility, with aluminum

completely avoided. Stainless steel was used for all metal components not used for heating. The stainless steel scissor lift initially had plastic spacers and a rubber handle, but these were all removed before use. Each gas line that could be in contact with the diborane is stainless steel, along with each connector or valve. One view port on the bell jar was replaced with a blank stainless steel flange. Each flange has a copper gasket for the seal. The MFCs use Kalrez, and each part of the pump that comes in contact with the gases is compatible. The materials used for the welding were verified to be compatible as well.

In case of a gas leak, plastic walls are mounted all around the system via Velcro. Diborane is slightly lighter than air, so if it leaks, it should float up. These plastic walls help guide any gas up to the upper part of the room, where it poses a much lower risk to personnel. Additionally, a diborane gas sensor and a hydrogen gas sensor are set up above the gas lines and chamber. The diborane sensor is powered by an RKI Beacon 800 Gas Detection Controller. A pressure gauge used on the system and the gas sensors are connected to a PC. This PC runs a LabVIEW program that monitors the pressure of the system and the gas sensors. If the pressure of the system gets too high (i.e., the pump stops working) or the sensors go off, the system kills power to the normally-closed solenoid valve attached to the diborane, which cuts off the gas flow.

An additional safety measure used is on the diborane gas line. The tank is located in a vented cabinet. Once the line is passed the solenoid valve, it is enclosed in a second stainless steel tubing by passing through a 1/4” to 1/2” connector, with a third connector used to exhaust anything in the second tube. The main gas line is 1/4” stainless steel tubing. A 1/2” stainless steel tube is placed around this tubing, with the two being bent together using a tube bender. Once this double-walled tubing goes through the plastic wall of the system, it goes through another 1/2” to 1/4” connector, taking the diborane line back to just the 1/4” tubing. A 3/8” fitting is also on this connector, with one of the nitrogen lines attached to this. A check valve is placed on the nitrogen line to prevent any backflow of diborane in case of a leak, and a filter regulator is also attached to this line to allow for pressure regulation. This allows for a flow of nitrogen into the 1/2” tubing that flows back to the vented cabinet. In the event of a leak, the diborane will then be pushed back to the vented cabinet via the nitrogen. This prevents any diborane from leaking into the atmosphere before the gas sensor. If there was a leak inside of the plastic walls, the diborane sensor and hydrogen sensor are there to detect anything. Figures 33 and 34 show the double-walled tubing.

Due to the currents and voltage being supplied, the entire system is grounded. Because the back of the power supply does not have any real enclosures to prevent personnel from shocking themselves, an enclosure was created with plastic to place over the back half of the power supply. If anything needs to be done to the power supply, the box can easily be removed, but the disconnect box should be turned off before doing this to ensure the power supply does not have power. Figure 35 shows the power supply with the plastic enclosure.

Figure 33: Double-walled tubing for the diborane.

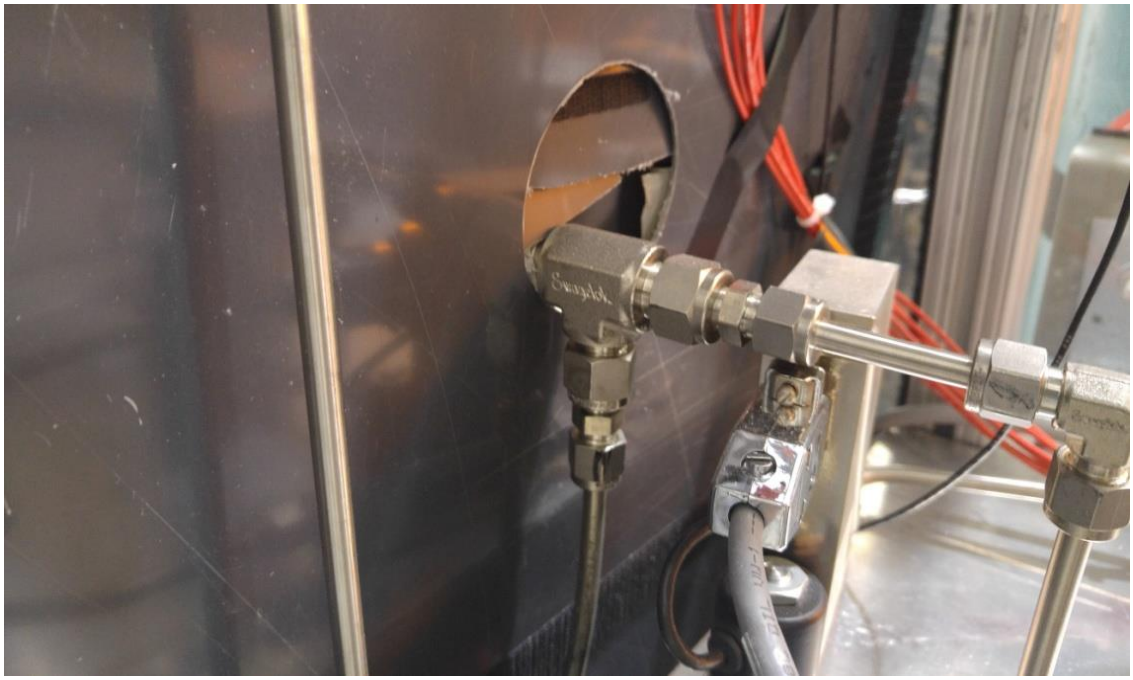

Figure 34: The double-walled tubing becomes just the 1/4” tube again.

Figure 35: Power supply with plastic enclosure to prevent shock hazard.

Growth Methodology

Before growths could be performed, several dry runs and tests were performed to get an idea of how to optimize the growth. Each gas line had heat tape applied to it to try and get rid of as much moisture as possible. The temperature of the tungsten filaments, as well as the surrounding area were investigated at various voltage and current values. Starting with low values for each and increasing, the temperatures were measured via a thermocouple feedthrough. With 3 V and 55 A, the filaments got up to around 300°C, and the substrate area got up to around 120°C. Increasing to approximately 12 V and 150 A resulted in filament temperatures being right around 1000°C, and the substrate area temperature being approximately 800°C. The filaments were all slightly different temperatures in each test case, but they all seemed to be within 5-10% of each other. A somewhat slow ramp-up to these values is required to avoid possible damage to the system. For each of these tests, the system was placed under vacuum to avoid oxidization concerns.

With the heating tests completed, the pump was investigated. This pump requires nitrogen when pumping, so it is important to not start a growth with a nitrogen tank that is low. In order to test how long a tank will last, a dry run was performed, with the nitrogen flowing to the pump and to the double-walled tubing containing the diborane. The tank emptied in around 8 hours, but it was not a completely full tank, as it had been used for carburization of the tungsten filaments and other tests. Because of this, a tank seems to last approximately 14 hours, assuming carburization is not being performed repeatedly. The chamber is purged with nitrogen after every growth, so this could result in varying times.

Before getting into the general methodology of the growths, a discussion of some early problems will be presented. A bake out was attempted before growing to get rid of as much moisture as possible, since diborane is highly reactive with water. While attempting this bake out, however, the chiller attached to the pump continued to produce

an error and stop working. This would result in the pump rapidly increasing in temperature. Several different things were attempted to fix it, but the problem persisted. It would sometimes error out within five minutes of turning on, and it would sometimes error out in twenty minutes. The error code said there was likely debris in the lines and explained where the reset button was for the error. Resetting the error would fix it temporarily, but the problem would still occur. Eventually, the filter for the chiller was changed just to see if that might help, and the error stopped occurring. With the chiller working, the bake out could be performed.

Once the bake out was performed, the growths could be performed. Unfortunately, during the first growth, the temperature around the substrate started to decrease after a certain point. The tungsten filaments stopped glowing, and the power supply was dropping in both current and voltage. Upon inspecting the chamber, one of the tungsten filaments apparently snapped in two during the heating and hit the boron nitride plate. This caused it to snap in two and created a mess in the chamber. After cleaning the chamber and replacing the boron nitride plate, another growth was attempted. This time, the substrate area was around 600°C when an audible pop could be heard, and, again, the temperature of the chamber started to drop rapidly, as did the current and voltage of the power supply. After inspecting the chamber, it appears that one of the copper wires used for the heating somehow broke loose and hit one of the boron nitride bars used to hold the copper bars, snapping it in two and creating another mess inside of the chamber. Figure 36 shows some of the damage that was done.

Figure 36: Boron nitride bar broken in two (silver wire is the thermocouple).

After replacing the boron nitride block and verifying that everything was securely connected, another growth was attempted. This time no errors occurred, and the growth was able to be completed. When looking at the film, it was very blue in color, which was not expected. It seems that the tungsten filaments were not carburized enough, resulting in deposition of tungsten on the substrate. After carburizing the filaments, another growth was attempted. Although there was not any blue on the substrate this time, there was also no real deposition on the substrate. A few more growths were attempted with similar results. It was determined that the thermocouple was actually reading the temperature of the filaments and not the substrate, resulting in temperatures that were too low to allow for deposition. Once this was corrected, growths were continued with actual depositions.

A very general procedure for a growth will now be presented. It may differ slightly from growth to growth, as parameters were tweaked, but each growth follows this general method. If needed, heat tape can be applied to each gas line, but this is only required if the non-nitrogen lines were disconnected for any reason. Unless the tungsten filaments need to be changed, carburization should not be required. The bell jar needs to be lifted to allow for the sample to be inserted into the chamber. Inspection of everything inside the chamber is paramount for safety, so a thorough inspection should be performed, while wearing gloves to avoid contamination. Assuming nothing needs to be fixed or changed, the sample can be placed on the boron nitride plate. The power supply and pump can then be turned on via their respective disconnect boxes. The chiller and nitrogen are turned on for the pump, and the system is placed under vacuum. Once the system is under vacuum, the power supply is turned on to begin heating up the chamber. Once the system gets to the desired temperature for growth, the hydrogen and methane can be allowed to flow via the MFCs, with the diborane being allowed after this. The temperature and pressure of the system are monitored while deposition occurs. After the growth is completed, the power supply is turned off, the MFCs are turned off via the controller, and the gas tanks are closed, except the nitrogen. The quarter-turn valve blocking the nitrogen from entering the chamber is opened to allow for purging of the chamber. With this completed, the quarter-turn valve should be closed again, and the pump can then be turned off, as well as the chiller and nitrogen. After cooling down, the sample is removed from the chamber.

The parameters used for a typical growth are presented in Table 1. These values may change slightly as the process is optimized, but this gives an idea of the values used for each parameter. The pressure increases slightly when the power supply starts heating the chamber, so the pressure it reaches after the power supply is turned on is reported.

Table 1: Typical parameters for deposition of boron carbide onto silicon wafers.

Parameter:	Value:
Gas Flow Rate (H_2)	35 sccm
Gas Flow Rate (CH_4)	50 sccm
Gas Flow Rate (B_2H_6)	10 sccm
Substrate Temperature	800-1000°C
Pressure	500 mTorr
Substrate to Filament Distance	6 mm
Deposition Time	2-3 hours

CHAPTER FOUR

RESULTS AND DISCUSSION

Before growing films, simulations were performed to get an idea of what to expect from the grown films and to get an idea of the necessary system parameters to achieve full depletion within the boron carbide layer. Monte Carlo N-Particle Transport Code (MCNP) was used to simulate a boron carbide detector, as well as a conversion layer silicon detector with boron carbide as the conversion layer. Silvaco was used to simulate the electric field profile in a B_4C-silicon detection system architecture. Because boron carbide is p-type, n-type silicon was selected for simulations to allow for a heterostructured diode with a boron carbide active layer. After actually growing films, they were looked at using a scanning electron microscope (SEM).

MCNP6 Simulations

MCNP6 simulations were performed to see the possible detection efficiency of a solid-state boron carbide detector at varying thicknesses. A cylinder was used for the boron carbide, and a cylinder made of silicon was placed underneath the boron carbide. For the normal simulation, a 20% isotopic amount of ^{10}B was selected. For the isotopically-enriched simulation, a 95% isotopic amount of ^{10}B was selected. The carbon content was selected to be at 20 at.% in each case. A plane wave of thermal neutrons (0.025 eV) was used for the simulations. The simulations started with a boron carbide thickness of 3 μm, with each case increasing in thickness by 2 μm until reaching a thickness of 101 μm. The silicon thickness was selected as a static 100 μm.

To acquire good statistics, 30,000,000 neutrons were simulated for each of these simulations. The detection efficiency for the solid-state boron carbide detector was defined as the number of neutron captures in the boron carbide divided by the total number of neutrons. Table 2 shows the detection efficiency of boron carbide at several different thicknesses with a zero threshold.

Table 2: Detection efficiency based on varying thicknesses of boron carbide on silicon with a zero threshold

	3 μm	15 μm	25 μm	55 μm	75 μm	95 μm
B_4C (%)	2.52	11.94	19.08	37.25	47.03	55.29
^{10}B-Enriched (%)	12.03	47.30	65.60	90.43	95.92	98.25

In the case of a conversion layer, it has been previously discussed that the range of the reaction products will ultimately limit the detection efficiency. The range of an alpha particle is approximately 3 μm in boron carbide, so the maximum detection efficiency of a single-sided boron carbide conversion layer detector is approximately

2.52% for natural boron carbide and 12.03% for ^{10}B-enriched boron carbide. For a solid-state boron carbide detector, the efficiency increases with increasing thickness of B_4C. For natural boron carbide, the efficiency reaches approximately 55% at a film thickness of 95 µm, while ^{10}B-enriched boron carbide approaches 100% efficiency at a film thickness of 95 µm. It appears that a film thickness of around 12 µm would result in a detection efficiency of 10% for natural boron carbide.

The pulse height spectra for three different thicknesses of natural boron carbide can be seen in Figure 37. Each of these show the expected peak at 2.31 MeV and 2.79 MeV. Increasing the thickness of the boron carbide allowed for the spectrum to flatten out, as the wall effect diminishes with increasing thickness. Figure 38 shows the same pulse height spectra as Figure 37, but with the addition of the pulse height spectra in the silicon at the same thickness. As previously discussed, conservation of momentum only allows one of the particles to be deposited into the silicon in this setup; therefore, the expected energy peaks are at around 0.84 MeV and 1.47 MeV. This can be seen in the silicon spectra, but as the thickness of the boron carbide is increased, the peak decreases. This is due to the fact that the reaction products start to be absorbed in the boron carbide, instead of the silicon.

Silvaco Simulations

Silvaco simulations were performed to determine band structures and electrical field profiles of the diodes with different doping and bias to compare with experimental results. The electron deficiency created by vacancy defects and point defects results in the generation of intrinsic defects formed as gap states inside of the band gap of the semiconductor. Such high concentrations of gap states attached to the valence band affect the electronic charge transport. Conclusively, the p-type character of the semiconductor is aroused [35]. Amongst all of the stable BC isotopes, B_4C was selected for simulations, as it is what is grown by the HFCVD; however, B_4C has rarely had its physical properties investigated. Therefore, the few experimentally known values were employed to conduct simulations. As previously discussed, there is a range of band gap values for boron carbide, depending on the carbon concentration. For simulation purposes, 0.9 eV was selected as the band gap, which was measured via optical absorption by Werheit [36]. Although 0.9 eV was used for the simulations, the band gap of the grown boron carbide should be closer to 2 eV, based on the resulting carbon concentration. The diode modeling in this study was based on the values of the doping concentration of B_4C from Hong et al. [37]. Table 3 shows all of the characteristics of the parameters used for the modeling. A schematic of the simulations can be seen in Figure 39.a, while Figure 39.b shows the energy band structure of the B_4C/n-Si heterostructure used in the Silvaco simulations. For this simulation, a thickness of B_4C and n-Si were selected as 100 µm and 500 µm, respectively. Aluminum was used for the metal contact to boron carbide. The simulation results showed the Al/B_4C contact created a rectifying contact, since the work function of B_4C is larger than that of Al. This feature was kept to continually simulate the other electrical properties.

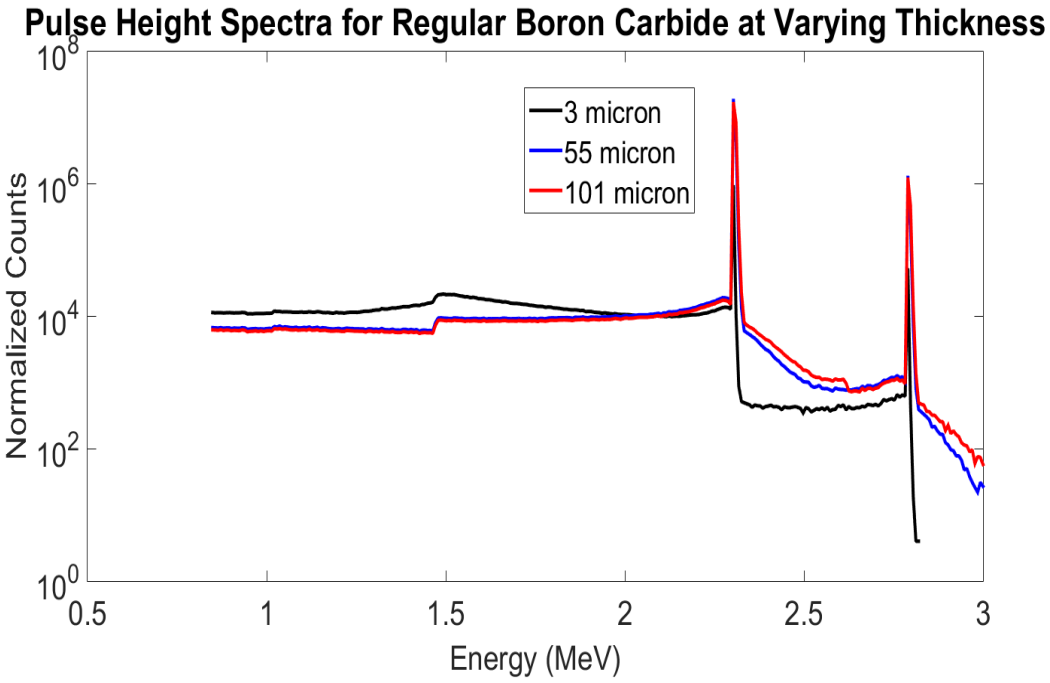

Figure 37: Pulse height spectra for three different thicknesses of (natural) boron carbide.

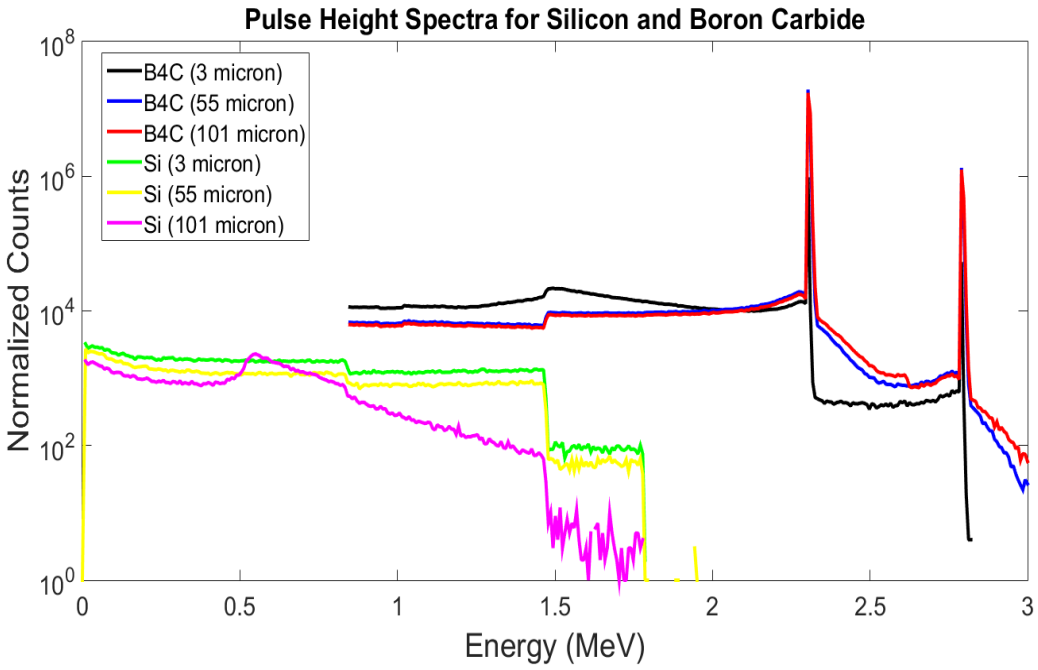

Figure 38: Pulse height spectra for the three different (natural) boron carbide thicknesses and the corresponding silicon pulse height spectra.

Table 3: Properties of B_4C that were used for Silvaco simulations in this study.

Characteristics:	Values:	Unit:
Band gap energy	0.9 at 300 K [18]	eV
Carrier lifetime	$1.0x10^{-8}$ [18]	Second
Dopant concentration	$4.2x10^{12}$ [37]	cm^{-3}
Mobility	electron: 0.001, hole: $7.5x10^{-4}$ [37]	cm^2/V-second

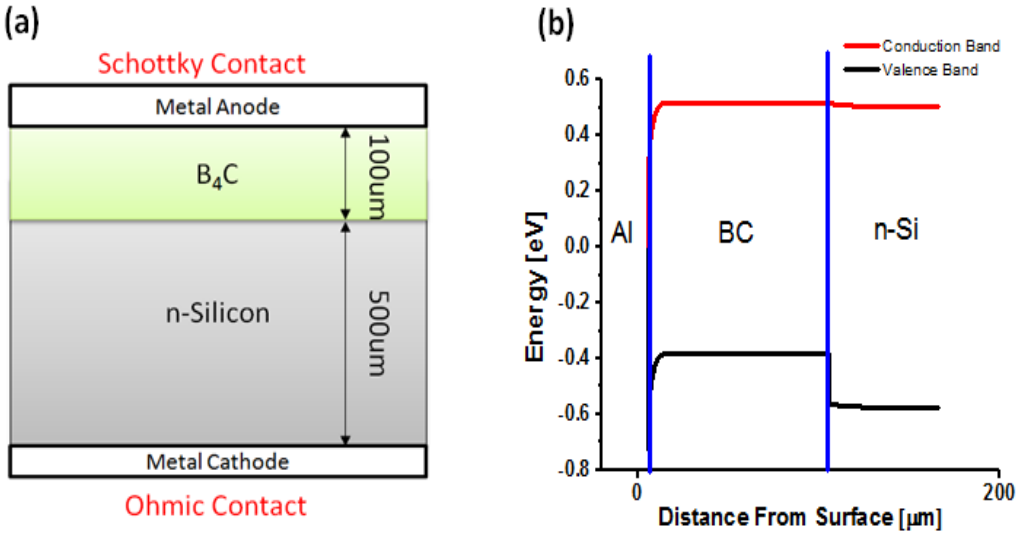

Figure 39: Schematic of the setup for the simulation (a) and the energy band structure (b).

From the simulations, it was found that the silicon must have a much higher free carrier concentration than the boron carbide to ensure that the junction resides mainly in the boron carbide layer. Figure 40 shows the electric field as a function of depth from the surface for one set of simulations. As Figure 40 shows, the necessary bias to obtain full depletion of the 100 μm thick boron carbide layer is only around 50 V in this system design. Using a properly designed blocking front contact, the electric field could be enhanced and flattened in the boron carbide, thereby maximizing charge collection.

Thin Film Analysis

The films appear to have a uniform deposition across the silicon wafers and appear dark gray or black in color. A Zeiss Auriga Focused Ion Beam Scanning Electron Microscope (FIB-SEM) was used to view the surface features of the grown samples. Van der Pauw and Hall measurements were performed on the deposited films to determine the resistivity, bulk carrier density, and Hall mobility. These measurements were performed with a printed circuit board (PCB) and a Keithley 2410 SourceMeter. XRD analysis was also performed on two samples to compare to expected results for B_4C. Alpha and neutron response were both tested for several different deposited films; however, there was a large source of noise for each test, indicating that the films may have had too much contamination on the surface.

SEM Imaging

Using the SEM, the surface of the samples could be seen to check for uniformity and abnormalities. Figures 41, 42, and 43 all show images from a 10 Ω-cm silicon wafer with boron carbide deposited onto it. Figure 41 seems to show a uniform deposition across the wafer, but there are some slight differences that can be seen. Figure 42 shows a closer look at the surface than Figure 41. This shows that there is at least some difference in film thickness across the wafer. This could have resulted from the wafer not being centered for the growth process. Figure 43 shows a closer image of the more elevated region to the left in Figure 42. As this image shows, it appears that this sample was polycrystalline or amorphous, instead of single-crystalline. This may have resulted from a deposition rate that was too fast, which could prevent a single-crystalline formation from occurring. A 10 kΩ-cm silicon wafer was also imaged with the SEM. Figure 44 shows the surface of the wafer with boron carbide deposited on it. Similar to the 10 Ω-cm wafer already discussed, the deposition appeared to be uniform across the surface; however, there were spots on the wafer that did not receive any deposition. This could be from the wafer being slightly out of place or from the gases not flowing onto that section of the substrate. Figure 44 seems to show a more pronounced difference in the film thickness than Figure 42. Zooming in on this section produced Figure 45. Like Figure 43, Figure 45 appears to suggest that this film is amorphous or polycrystalline. Because both samples were amorphous or polycrystalline, instead of single-crystalline, it is likely that either the deposition rate was too fast or the substrate was too far from the filaments.

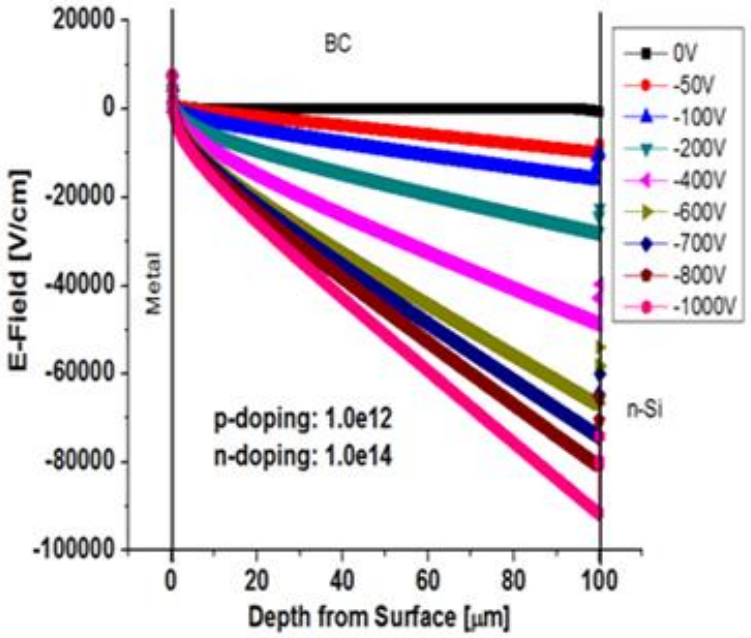

Figure 40: The electric field as a function of depth from the surface for one set of simulations.

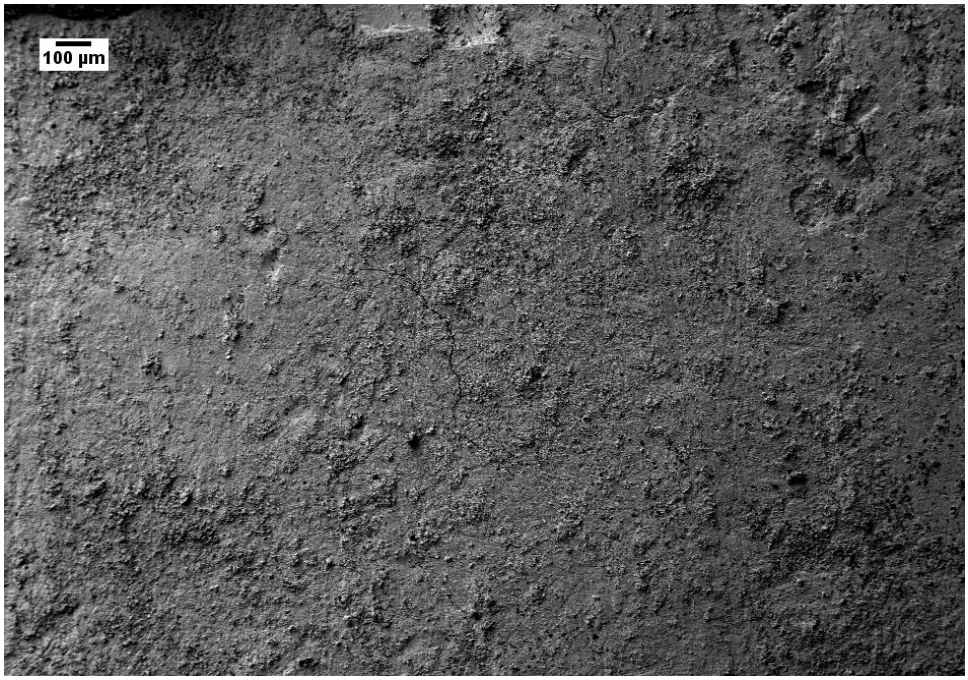

Figure 41: SEM image of 10 Ω-cm silicon wafer with thin film of boron carbide.

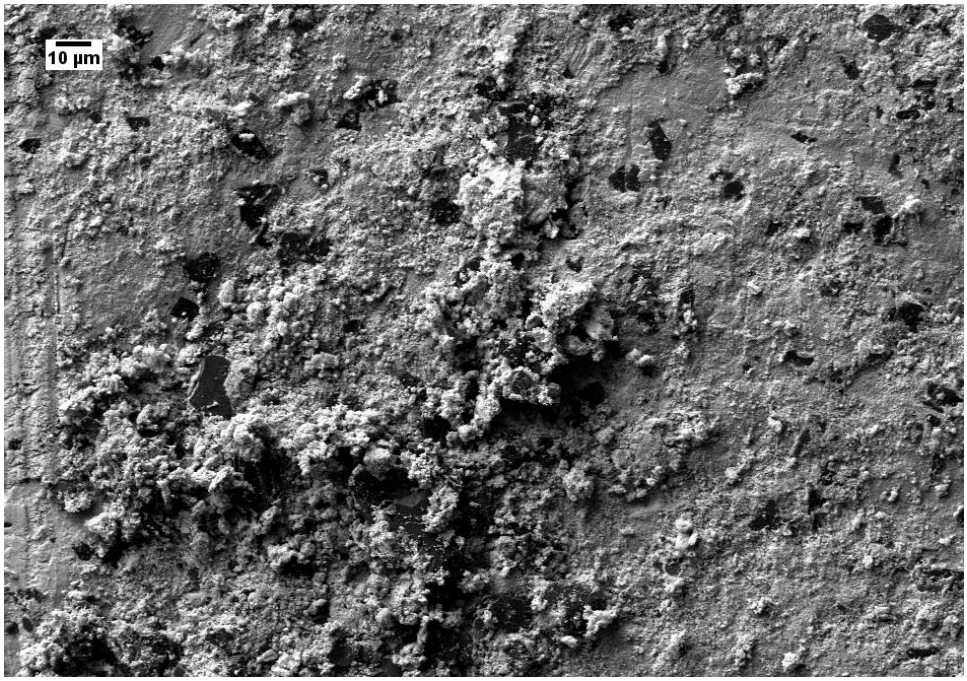

Figure 42: Closer SEM image of 10 Ω-cm silicon wafer with thin film of boron carbide.

Figure 43: Closer SEM image of boron carbide on 10 Ω-cm silicon. This image suggests a polycrystalline or amorphous film, rather than single-crystalline.

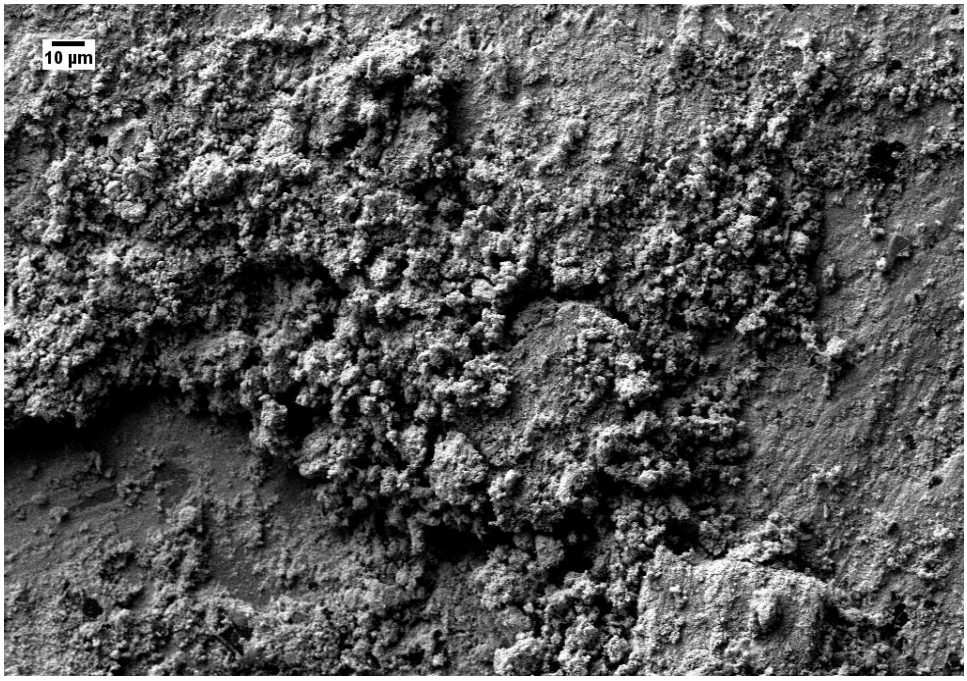

Figure 44: SEM image of 10 kΩ-cm silicon with film of boron carbide.

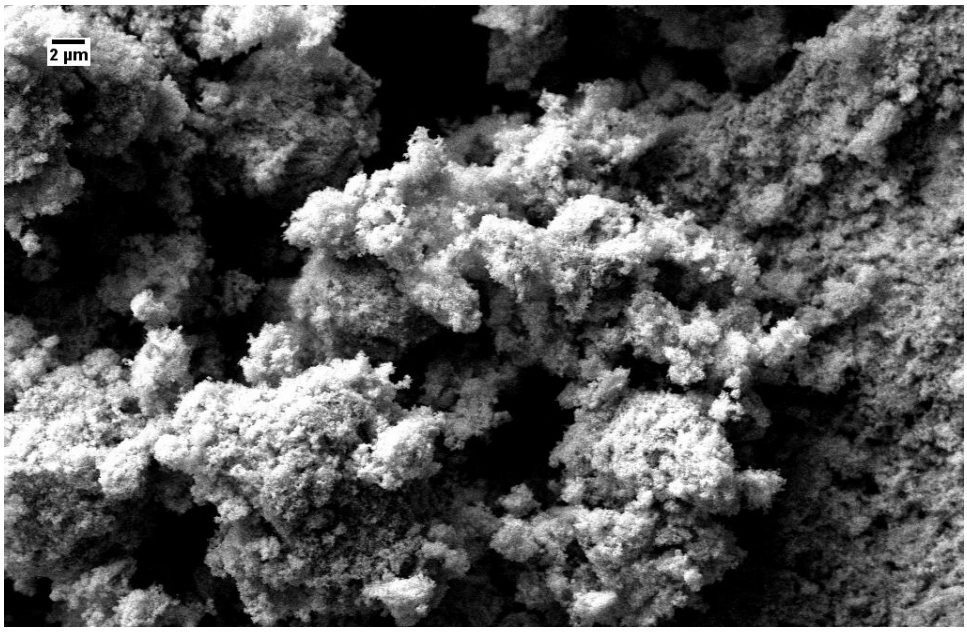

Figure 45: SEM image of 10 kΩ-cm silicon with film of boron carbide. This image again suggests a polycrystalline or amorphous film, instead of single-crystalline.

Van der Pauw and Hall Measurements

The van der Pauw method can be used to determine the specific resistivity of an arbitrary shape without knowing the current pattern, assuming that several different conditions are satisfied. These conditions are the following: the contacts are sufficiently small, the contacts are at the circumference of the sample, the sample is homogeneous in thickness, and the surface of the sample does not have isolated holes [38]. In particular, the average diameters of the contacts and sample thickness must be much smaller than the distance between the contacts [39]. The measurements are performed by sourcing a voltage across two of the sample corners and measuring the resulting current from the other two corners. This is done for a range of voltage values, and eight different combinations are used. Because half of the combinations are redundant, a check of measurement consistency can be performed. If any of the measurement checks differ by more than 5%, there is likely a source of error that needs to be identified. Characteristic resistances, R_A and R_B, are found from the inverse of the slopes of these combinations when plotted as current vs. voltage. Once these values are obtained, MATLAB can be used to solve for the sheet resistance (R_S), which can then give the resistivity of the sample. A numerical approach is used to solve for R_S because both R_A and R_B are known. The following equation is used in an iterative process to find R_S [39]:

$$\exp\left(-\pi * \frac{R_A}{R_S}\right) + \exp\left(-\pi * \frac{R_B}{R_S}\right) = 1$$

In order to verify the results from the experimental setup, measurements were performed on silicon substrates as well. Two different silicon substrates with a resistivity >10,000 Ω-cm were used for this check. Each sample was cleaned with acetone, isopropyl alcohol (IPA), and de-ionized water before performing the measurements to eliminate as much contamination as possible. Once cleaned, the samples were placed on a PCB, with each corner of the sample connected to the board via a spring clip. For the first silicon substrate, the resistivity was shown to be around 16,000 Ω-cm. For the second silicon substrate, the resistivity was shown to be around 25,500 Ω-cm. These were slightly different from one another, but this could be from oxidation on the substrates or some sort of contamination. While not exactly the same, this seems to indicate that the system gives accurate results. For the thin films deposited on the 10 Ω-cm substrates, the bulk resistivity was approximately 4,300 Ω-cm. Each film was slightly different, but they were all around this value. For the thin films deposited on the 10,000 Ω-cm substrates, the bulk resistivity was approximately 5,700 Ω-cm. Again, each film was slightly different, but they were all around this value. There are likely differences due to contamination or due to the higher resistivity of the 10,000 Ω-cm silicon substrates.

Literature shows a wide range of conductivity for boron carbide, depending on carbon concentration, method of preparation, and purity [18, 40, 41]. Plasma-enhanced CVD seems to produce extremely small conductivities, on the range of 10^{-4} to 10^{-10} Ω^{-1}-cm^{-1}, possibly due to very little free carbon being present [18]. Increasing the carbon

concentration appears to decrease the conductivity. Based on the results discussed above, the thin films grown on 10 Ω-cm substrates have a conductivity of approximately $2.33x10^{-4}$ Ω^{-1}-cm^{-1}, and the films grown on 10,000 Ω-cm substrates have a conductivity of approximately $1.75x10^{-4}$ Ω^{-1}-cm^{-1}. This is a little lower than expected, as literature shows conductivities several magnitudes higher than this at room temperature [18, 40, 41]. These values could be this small because there is a small amount of free carbon in the thin films, as a higher amount of free carbon will increase the conductivity.

After obtaining the resistivity of the samples, the sheet carrier density, bulk carrier density, and Hall mobility of the deposited films can be found. A custom-built Hall measurement system was used to determine these values. An iron yoke was created by welding together iron, leaving a gap big enough for two neodymium magnets and the PCB used for measurements. The resulting magnetic field with the magnets in place on the iron yoke is roughly 12,000 gauss. For the Hall measurements, a current is applied across opposite sample corners, and the resulting voltage from the other two corners is recorded. Once each measurement combination is done, the magnetic field is reversed, and the same procedure is performed. With these measurements, the sample type can be determined based on the sign of the voltage sum. The voltage sum is found by subtracting the values for the negative magnetic field from the corresponding values for the positive magnetic field and then adding the four values together. The sheet carrier density, bulk carrier density, and Hall mobility are then found from the following equations, where p_s is the sheet carrier density, n_s is the sheet carrier density, n is the bulk carrier density, p is the bulk carrier density, and μ is the Hall mobility [39]:

$$p_s = \frac{8x10^{-8}IB}{[q(V_C + V_D + V_E + V_F)]} \quad (if\ voltage\ sum\ is\ positive)$$

$$n_s = \left|\frac{8x10^{-8}IB}{[q(V_C + V_D + V_E + V_F)]}\right| \quad (if\ voltage\ sum\ is\ negative)$$

$$n = \frac{n_s}{d}$$

$$p = \frac{p_s}{d}$$

$$\mu = \frac{1}{qn_sR_S} \ \ or\ \mu = \frac{1}{qp_sR_S}$$

Hall measurements were performed on an n-type, 10 Ω-cm silicon substrate that had not been used for a growth to verify that the values were within reason. For the 10 Ω-cm substrate, the resistivity came out to be 76.4 Ω-cm, the bulk carrier density came out to be approximately $1.05x10^{14}$ cm^{-3}, and the Hall mobility came out to be 775 $cm^2V^{-1}s^{-1}$. The measurement resulted in a voltage indicating that the material is n-type. Using an online resistivity and mobility calculator for silicon with a bulk carrier density of $1.05x10^{14}$ cm^{-3} results in a mobility of 1,400 $cm^2V^{-1}s^{-1}$ and a resistivity of 42 Ω-cm. The

mobility is nearly twice what was measured, and the resistivity is nearly half of what was measured. This may be from contamination on the silicon.

10 Ω-cm and 10,000 Ω-cm silicon substrates with deposited B_4C were used for the Hall measurements. For each of these cases, two different samples were used to get measurements. For the thin films grown on the 10 Ω-cm substrates, the bulk carrier density came out to be approximately $5.68x10^{13}$ cm^{-3} and $4.78x10^{13}$ cm^{-3}. The Hall mobility came out to be 2.48 $cm^2V^{-1}s^{-1}$ and 3.06 $cm^2V^{-1}s^{-1}$, respectively. For the thin films grown on the 10,000 Ω-cm substrates, the bulk carrier density came out to be approximately $4.62x10^{13}$ cm^{-3} and $5.33x10^{13}$ cm^{-3}. The Hall mobility came out to be 23.3 $cm^2V^{-1}s^{-1}$ and 20.3 $cm^2V^{-1}s^{-1}$, respectively. These are slightly higher than the values used in Table 4, but this could be from contamination or from the silicon substrates themselves. For all of these, the measurement resulted in a voltage indicating that the material is p-type. Based on the work by Wood and Emin, the Hall mobility of boron carbide ranges from 0.1 to around 1 $cm^2V^{-1}s^{-1}$ [41]. The values for the 10 Ω-cm substrates is close to 1; however, the 10 kΩ-cm substrate values are a magnitude higher. This may be from the silicon itself, as the films are thin (4 micron). Although boron carbide is p-type, the Hall effect is n-type at very low carbon content [41]. Table 4 summarizes the results for the cases discussed.

Table 4: Results from van der Pauw and Hall measurements for several different thin films and a Si substrate.

	10 Ω-cm Si	10 Ω-cm Si (B_4C)	10 Ω-cm Si (B_4C)	10 kΩ-cm Si (B_4C)	10 kΩ-cm Si (B_4C)
n-type or p-type:	n-type	p-type	p-type	p-type	p-type
Bulk Resistivity:	76.4	4,428	4,270	5,783	5,790
Bulk Carrier Density:	$1.05x10^{14}$	$5.68x10^{13}$	$4.78x10^{13}$	$5.33x10^{13}$	$4.62x10^{13}$
Hall Mobility:	775	2.48	3.06	20.3	23.3

XRD Analysis

XRD was used to determine if the films are single-crystalline, polycrystalline, or amorphous. Figure 46 shows an XRD analysis of boron carbide from Alizadeh, Taheri-Nassaj, and Ehsani [42]. Figure 47 shows an XRD analysis of boron nitride from Zhong et al. [43]. The boron carbide has many different peaks, with it showing 17 total B_4C peaks and one peak for free carbon. These peaks are all quite narrow, with the free carbon being the broadest. The boron nitride only has four peaks. Again, these peaks are quite narrow.

Figure 48 shows the XRD analysis for a 10 Ω-cm film. The narrow peaks seen at 70° and approximately 28° are silicon peaks, and the narrow peak at around 26° is likely free carbon. Other than the silicon peaks and free carbon, the rest of the peaks appear to be very broad, likely from nanoparticles being present in the films. There are peaks at around 22°, 34°, 41°, 50°, and 55°. Because the peaks are so broad, it is possible that there are multiple peaks within these. Compared to Figure 46, it appears that these peaks could correspond to boron carbide; however, a few of the peaks (e.g., the peak at 41° and 55°) could also be from boron nitride contamination from the showerhead of the HFCVD system. Due to this possible contamination and nanoparticles, it is unclear if all the expected peaks are present. Figure 49 shows a second XRD analysis performed with a different film. This analysis was performed with a more accurate machine. With this scan, the silicon peaks disappeared, but the peaks appeared to get a little broader. The broad peak at around 24° appears to show two different peaks, one around 22° and one around 24°. There are other peaks at approximately 28°, 34°, 41°, 50°, 55°, and 60°. Compared to Figure 46, these peaks could still correspond to boron carbide, but the broadness of the peaks again makes it unclear. Figure 47 shows that boron nitride has a peak at around 26°, which could overlap with the boron carbide and free carbon peaks expected because the peaks are so broad. Because peaks were seen with both XRD analyses, it can be determined that the films are not single-crystalline. These films are polycrystalline instead. The XRD analysis shows that the growth process needs to be refined and contamination needs to be eliminated to be able to produce single-crystalline films.

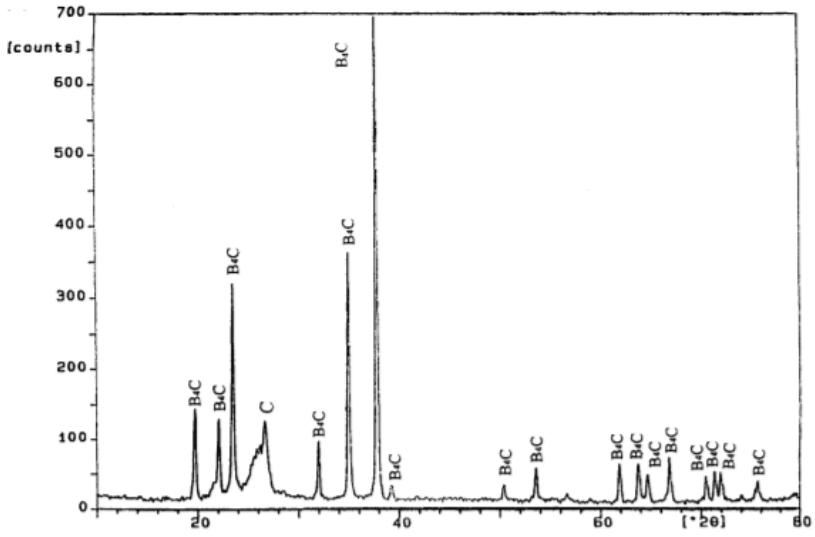

Figure 46: XRD analysis of boron carbide [42].

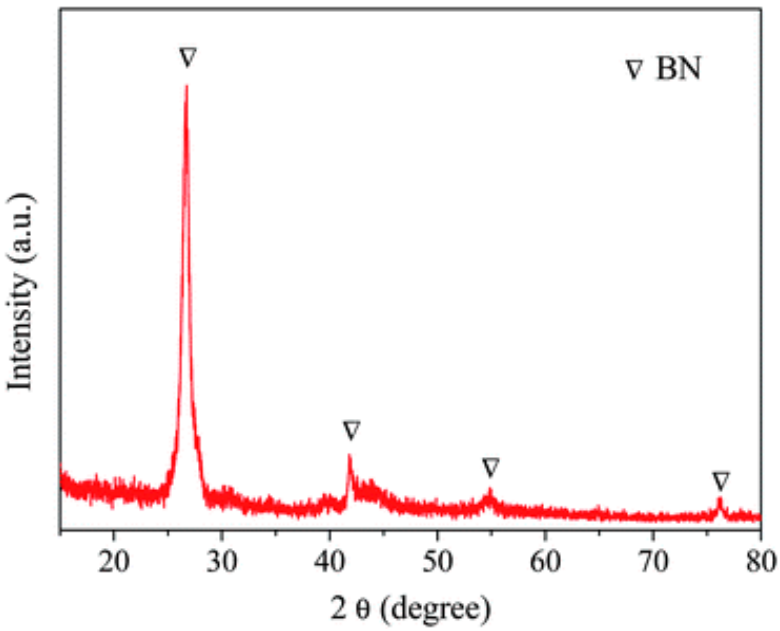

Figure 47: XRD analysis of boron nitride [43].

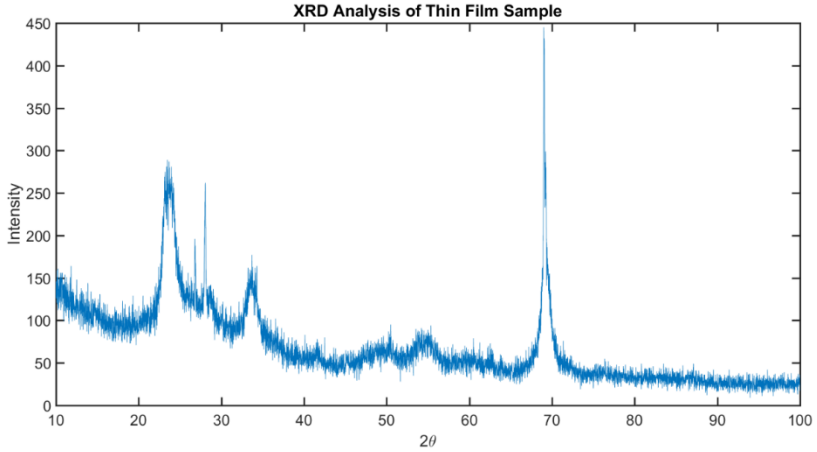

Figure 48: XRD analysis of boron carbide thin film.

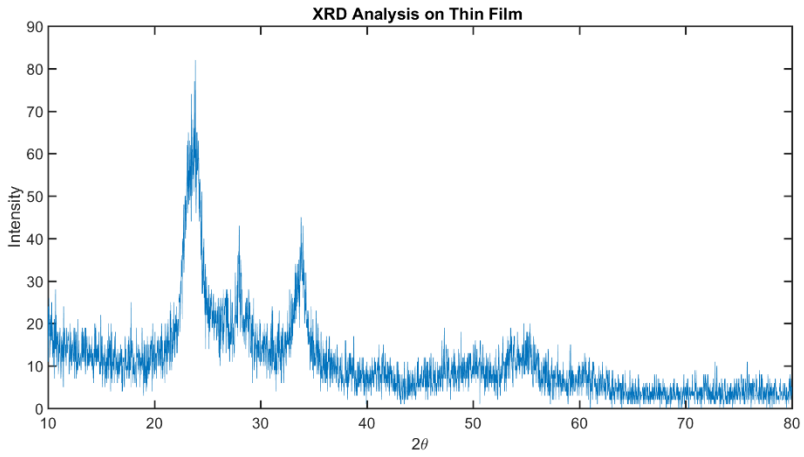

Figure 49: XRD analysis of boron carbide without silicon peaks

CHAPTER FIVE

CONCLUSIONS AND FUTURE WORK

Boron carbide films have been grown using a custom-built HFCVD system. The system was designed to be used with diborane as one of the reactant gases, so stainless steel was used wherever possible. Safety was a top priority in the design and construction of this system. Double-walled tubing is used for the diborane line, and gas sensors are connected to a PC to allow for automated shutdown of the system should a gas leak or system abnormality occur. A pressure gauge and thermocouple were both installed on the system in order to monitor conditions of the system during the growth process. Substrate temperatures of 800-1000°C were used for the deposition of the boron carbide onto the n-type silicon wafers. An SEM was used to image the grown samples. The deposition appeared to be uniform across the wafer, but there were differences when magnified. Van der Pauw and Hall measurements were performed to determine the resistivity, bulk carrier density, and the Hall mobility of the thin films. The Hall mobility was slightly higher than expected, indicating contamination or growth parameter issues. XRD analysis was performed to see if the films were single-crystalline. Unfortunately, the films appeared to be polycrystalline, indicating that further optimization of the growth process is required to produce single-crystalline boron carbide deposited onto the silicon wafers. Radiation detection was not possible with these samples, as there was a large amount of noise in each sample tested. This is likely due to contamination of some sort—possibly boron nitride contamination.

Future work consists of further optimization of the system and growth parameters, as deposition of single-crystalline boron carbide is desired. A design change to an inverted chimney reactor using a graphite susceptor is currently being investigated. Other analysis techniques will be performed on the grown films, including transmission electron microscopy (TEM), energy dispersive spectroscopy (EDS), laser-induced breakdown spectroscopy (LIBS), and Raman spectroscopy. Once a proper film has been grown, a boron carbide Schottky diode p-n heterojunction device will be created and tested for alpha and neutron response.

REFERENCES

1. Domnich, V., et al., *Boron Carbide: Structure, Properties, and Stability under Stress.* Journal of the American Ceramic Society, 2011. **94**(11): p. 3605-3628.
2. Suri, A.K., et al., *Synthesis and consolidation of boron carbide: a review.* International Materials Reviews, 2010. **55**(1): p. 4-40.
3. Sezer, A. and J.I. Brand, *Chemical vapor deposition of boron carbide.* Materials Science and Engineering: B, 2001. **79**: p. 191-202.
4. Crane, T.W. and M.P. Baker. *Neutron Detectors*. Available from: http://www.lanl.gov/orgs/n/n1/panda/00326408.pdf.
5. Knoll, G.F., *Radiation Detection and Measurement*. 4th ed. 2010, New Jersey: Wiley.
6. Neamen, D.A., *Semiconductor physics and devices: basic principles*. 2003: McGraw-Hill.
7. Aselage, T.L. and R.G. Tissot, *Lattice Constants of Boron Carbides.* Journal of the American Ceramic Society, 1992. **75**(8): p. 2207-2212.
8. Yardley, J. *Silicon Basics -- General Overview*. Available from: https://www1.columbia.edu/sec/itc/ee/test2/pdf%20files/silicon%20basics.pdf.
9. Chaudhari, P., et al., *Fabrication and characterization of silicon based thermal neutron detector with hot wire chemical vapor deposited boron carbide converter.* Nuclear Instruments and Methods in Physics Research Section A: Accelerators, Spectrometers, Detectors and Associated Equipment, 2015. **779**: p. 33-38.
10. Robertson, B.W., et al., *A class of boron-rich solid-state neutron detectors.* Applied Physics Letters, 2002. **80**(19): p. 3644.
11. Ohring, M., *Materials Science of Thin Films Deposition and Structure*. 2002: Academic Press.
12. Vandenbulcke, L. and G. Vuillard, *Composition and structural changes of boron carbides deposited by chemical vapor deposition under various conditions of temperature and supersaturation.* Journal of the Less-Common Metals, 1981. **82**: p. 49-56.
13. Niihara, K., A. Nakahira, and T. Hirai, *The Effect of Stoichiometry on Mechanical Properties of Boron Carbide.* Journal of the American Ceramic Society, 1984. **67**(1): p. C-13-C-14.
14. Kevill, D., et al., *Preparation of boron-carbon compounds, including crystalline B2C material, by chemical vapor deposition.* Journal of Less-Common Metals, 1986. **117**: p. 421-425.
15. Jansson, U., J.O. Carlsson, and B. Stridh, *Initial stages of growth during boron carbide chemical vapor deposition.* Journal of Vacuum Science & Technology A, 1987. **5**(5): p. 2823-2828.
16. Jansson, U., et al., *Chemical vapour deposition of boron carbides I: phase and chemical composition.* Thin Solid Films, 1989. **172**: p. 81-93.
17. Chaudhari, P., et al., *Hot wire chemical vapor deposited boron carbide thin film/crystalline silicon diode for neutron detection application.* Solid-State Electronics, 2012. **78**: p. 156-158.

18. Lee, S., et al., *Characterization of boron carbide thin films fabricated by plasma enhanced chemical vapor deposition from boranes.* Journal of Applied Physics, 1992. **72**(10): p. 4925-4933.
19. Lee, S., et al., *The structural homogeneity of boron carbide thin films fabricated using plasma-enhanced chemical vapor deposition from B5H9+CH4.* Journal of Applied Physics, 1993. **74**(11): p. 6919-6924.
20. Komatsu, S. and Y. Moriyoshi, *Simultaneous growth of rhombohedral and amorphous boron films in a low pressure B2H6+H2+He plasma.* Journal of Crystal Growth, 1988. **89**(4): p. 560-570.
21. Komatsu, S. and Y. Moriyoshi, *Transition from amorphous to crystal growth of boron films in plasma-enhanced chemical vapor deposition with B2H6+He.* Journal of Applied Physics, 1989. **66**(1): p. 466-469.
22. Künzli, H., et al., *Influence of B2H6/CH4 and B(CH3)3 as process gas on boron carbide coatings: an insitu photoelectron spectroscopy study.* Journal of Nuclear Materials, 1992: p. 622-626.
23. Zhang, D., et al., *Growth and Characterization of Boron Carbide Nanowires.* Journal of Materials Science Letters, 1999. **18**(5): p. 349-351.
24. Liu, Y., et al., *Uniform design and regression analysis of LPCVD boron carbide from BCl3-CH4-H2 system.* Applied Surface Science, 2009. **255**: p. 5729-5735.
25. Guan, Z., *Boron carbide nanowires: Synthesis and characterization*. 2013, The University of North Carolina at Charlotte: Ann Arbor. p. 121.
26. Pallier, C., et al., *Structure of an Amorphous Boron Carbide Film: An Experimental and Computational Approach.* Chemistry of Materials, 2013. **25**(13): p. 2618-2629.
27. Airgas. *Boron Trichloride [Material Safety Data Sheet]*. Available from: https://www.airgas.com/msds/001005.pdf.
28. Airgas. *Diborane [Material Safety Data Sheet]*. Available from: http://louisville.edu/micronano/files/documents/material-safety-data-sheets-msds/Diborane.pdf.
29. Gómez-Aleixandre, C., et al., *Influence of Diborane Flow Rate on the Structure and Stability of CVD Boron Nitride Films.* The Journal of Physical Chemistry, 1996. **100**(6): p. 2148-2153.
30. Pierson, H.O. and A.W. Mullendore, *The chemical vapor deposition of TiB2 from diborane.* Thin Solid Films, 1980. **72**(3): p. 511-516.
31. Davis, J.W. and S. Fabritsiev, *Pure Tungsten - Electrical Resistivity*, in *ITER Material Properties Handbook*.
32. Youel, K.J., et al., *Diborane Handbook*. 1970.
33. Gases, B. *Diborane [Material Safety Data Sheet]*. 1995.
34. Praxair. *Diborane [Material Safety Data Sheet]*. 2009; Available from: http://www.praxair.com/~/media/North%20America/US/Documents/SDS/Diborane%20B2H6%20Safety%20Data%20Sheet%20SDS%20P4586.ashx.
35. Zuppiroli, L., N. Papandreou, and R. Kormann, *The dielectric response of boron carbide due to hopping conduction.* Journal of Applied Physics, 1991. **70**(1): p. 246-252.

36. Werheit, H., *On excitons and other gap states in boron carbide.* Journal of Physics: Condensed Matter, 2006. **18**(47): p. 10655.
37. Nina, H., et al., *Boron carbide based solid state neutron detectors: the effects of bias and time constant on detection efficiency.* Journal of Physics D: Applied Physics, 2010. **43**(27): p. 275101.
38. van der PAUYV, L., *A method of measuring specific resistivity and Hall effect of discs of arbitrary shape.* Philips Res. Rep, 1958. **13**: p. 1-9.
39. Thurber, R. *Resistivity and Hall Measurements*. 2010 2016; Available from: https://www.nist.gov/pml/engineering-physics-division/resistivity-and-hall-measurements#definitions.
40. Bandyopadhyay, A.K., et al., *The role of free carbon in the transport and magnetic properties of boron carbide.* Journal of Physics and Chemistry of Solids, 1984. **45**(2): p. 207-214.
41. Wood, C. and D. Emin, *Conduction mechanism in boron carbide.* Physical Review B, 1984. **29**(8): p. 4582-4587.
42. Alizadeh, A., E. Taheri-Nassaj, and N. Ehsani, *Synthesis of boron carbide powder by a carbothermic reduction method.* Journal of the European Ceramic Society, 2004. **24**(10–11): p. 3227-3234.
43. Zhong, B., et al., *Hollow BN microspheres constructed by nanoplates: synthesis, growth mechanism and cathodoluminescence property.* CrystEngComm, 2011. **13**(3): p. 819-826.

VITA

Dylan Richardson was born in Knoxville, TN on May 19, 1992. He attended McMinn County High School in Athens, TN, where he graduated valedictorian. Dylan enrolled at the University of Tennessee at Knoxville in the 2010 fall semester. He initially majored in biomedical engineering, but switched to nuclear engineering at the end of his sophomore year. During his undergraduate career, Dylan worked as an undergraduate research assistant for Dr. Eric Lukosi, where he worked with lithium indium diselinide. He graduated Summa Cum Laude with his Bachelor of Science degree in Nuclear Engineering in May of 2014. He then continued his education at the University of Tennessee at Knoxville as a Graduate Research Assistant in order to obtain his Master of Science and PhD in nuclear engineering. Dylan plans to graduate with his Master of Science in May 2017 and to continue his education to obtain a PhD in nuclear engineering. He will also be marrying his fiancée, Alyssa Wall, in May 2017.